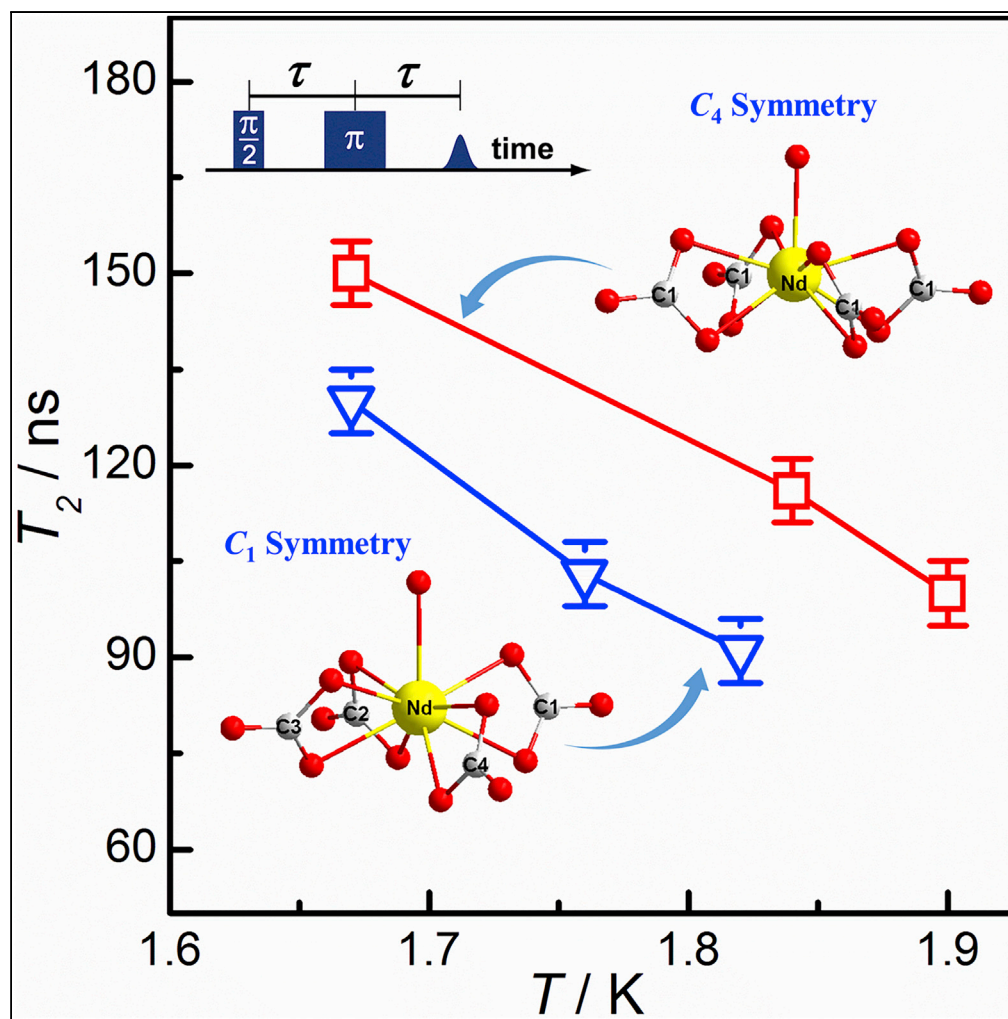## Article

Controlling Electron Spin Decoherence in Nd-based Complexes via Symmetry Selection

Jing Li, Lei Yin, Shi-Jie Xiong, ..., Johan van Tol, You Song, Zhenxing Wang

zhangyiquan@njnu.edu.cn (Y.-Q.Z.)
vantol@magnet.fsu.edu (J.v.T.)
yousong@nju.edu.cn (Y.S.)
zxwang@hust.edu.cn (Z.W.)

HIGHLIGHTS

Neodymium-based complexes show the spin decoherence without the magnetic dilution

The higher structural symmetry results in longer spin decoherence times

The phonon bottleneck effect induces the slow magnetization relaxation behaviors

Article

Controlling Electron Spin Decoherence in Nd-based Complexes via Symmetry Selection

Jing Li,[2,6] Lei Yin,[1,6] Shi-Jie Xiong,[5] Xing-Long Wu,[5] Fei Yu,[2] Zhong-Wen Ouyang,[1] Zheng-Cai Xia,[1] Yi-Quan Zhang,[4,*] Johan van Tol,[3,*] You Song,[2,*] and Zhenxing Wang[1,7,*]

SUMMARY

Long decoherence time is a key consideration for molecular magnets in the application of the quantum computation. Although previous studies have shown that the local symmetry of spin carriers plays a crucial part in the spin-lattice relaxation process, its role in the spin decoherence is still unclear. Herein, two nine-coordinated capped square antiprism neodymium moieties $[Nd(CO_3)_4H_2O]^{5-}$ with slightly different local symmetries, C_1 versus C_4 (1 and 2), are reported, which feature in the easy-plane magnetic anisotropy as shown by the high-frequency electron paramagnetic resonance (HF-EPR) studies. Detailed analysis of the relaxation time suggests that the phonon bottleneck effect is essential to the magnetic relaxation in the crystalline samples of 1 and 2. The 240 GHz Pulsed EPR studies show that the higher symmetry results in longer decoherence times, which is supported by the first principle calculations.

INTRODUCTION

Single-molecule magnets (SMMs) (Sessoli et al., 1993) are promising candidates as the quantum bits (qubits), the basic building blocks of a quantum computer according to Leuenberger and Loss's proposal (Leuenberger and Loss, 2001), in which they show slow spin relaxation behaviors between the bistable ground states with an energy barrier. However, the large zero-field splittings of SMMs result in low population in high-energy levels at low temperatures, which hinders the application of SMMs as qubits (Takahashi et al., 2008, 2009; 2011; Wang et al., 2011). In recent years, there has been a drive to achieve smaller energy splittings using the mesoscopic spin states produced by hyperfine interactions between the electron and nuclear spins as a substitution, which are termed as qudits (Aguila et al., 2014; Atzori et al., 2016a, 2016b, 2017; Fataftah et al., 2016; Graham et al., 2014; Martinez-Perez et al., 2012; Pedersen et al., 2016; Shiddiq et al., 2016; Tesi et al., 2016; Thiele et al., 2014; Yu et al., 2016; Zadrozny et al., 2017). Yet, the strong decoherence must be overcome to implement the envisaged application. Specific design criteria, such as nuclear-spin-free ligands (Yu et al., 2016), clock transitions (Zadrozny et al., 2017; Shiddiq et al., 2016), and low-energy vibrations (Atzori et al., 2017) have been developed to improve the quantum coherence time and temperature. As a matter of fact, the symmetry plays a vital part in spin-lattice relaxation process (namely, T_1) (Ding et al., 2016). Consequently, it is very probable that the local symmetry of a spin carrier is equally important to the spin-spin relaxation process (namely, T_2). However, the relationship between the decoherence and the local symmetries of spin carriers is still unclear.

Sessoli (Atzori et al., 2016a, 2016b, 2017; Tesi et al., 2016) and Freedman (Fataftah et al., 2016; Graham et al., 2014; Yu et al., 2016; Zadrozny et al., 2017) have contributed greatly to the development of molecular qubits with 3d transition metal ions as spin carriers. Nevertheless, up to now, only a few 4f metal centers showing the quantum coherence properties (Aguila et al., 2014; Pedersen et al., 2016; Martinez-Perez et al., 2012; Thiele et al., 2014; Shiddiq et al., 2016) have been reported. Herein, we report two capped square antiprism neodymium complexes, $[C(NH_2)_3]_5[Nd(CO_3)_4H_2O] \cdot 2H_2O$ (1) and $[C(NH_2)_3]_4[H_3O][Nd(CO_3)_4H_2O] \cdot 9.5H_2O$ (2), which have different local symmetries, C_1 (1) versus C_4 (2), in the neodymium moieties $[Nd(CO_3)_4H_2O]^{5-}$. Both neodymium-based complexes are easy-plane magnetic anisotropic and show field-induced slow magnetic relaxation behaviors, which is rare in lanthanide complexes. The quantum coherence phenomenon was observed by the 240 GHz pulsed EPR spectroscopies at low temperatures on undiluted complexes. Our work indicates that the higher symmetry results in the longer decoherence times, which is explained by the first principle calculations.

RESULTS AND DISCUSSIONS

X-Ray Structural Studies

Complexes 1 and 2 were synthesized according to a modified method reported with different rare-earth salts (Runde et al., 2000; Goff et al., 2010). The single crystal XRD reveals that 1 and 2 crystallize in the orthorhombic

[1]Wuhan National High Magnetic Field Center & School of Physics, Huazhong University of Science and Technology, Wuhan 430074, P. R. China

[2]State Key Laboratory of Coordination Chemistry, School of Chemistry and Chemical Engineering, Nanjing University, Nanjing 210023, P. R. China

[3]National High Magnetic Field Laboratory, Florida State University, Tallahassee, FL 32310, USA

[4]Jiangsu Key Laboratory for NSLSCS, School of Physical Science and Technology, Nanjing Normal University, Nanjing 210023, P. R. China

[5]National Laboratory of Solid State Microstructures and Department of Physics, Nanjing University, Nanjing 210093, P. R. China
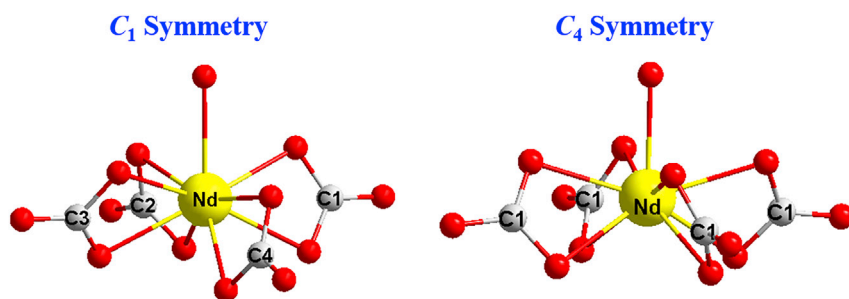
[6]These authors contributed equally

[7]Lead Contact

*Correspondence:
zhangyiquan@njnu.edu.cn
(Y.-Q.Z.),
vantol@magnet.fsu.edu
(J.v.T.),
yousong@nju.edu.cn (Y.S.),
zxwang@hust.edu.cn (Z.W.)
https://doi.org/10.1016/j.isci.
2020.100926

Figure 1. The Structures of 1 and 2

Crystallographically determined molecular structure of the $[Nd(CO_3)_4(H_2O)]^{5-}$ anion of **1** (left) and **2** (right). Neodymium, yellow; oxygen, red; carbon, gray. See also Figures S1, S2, S16, and S17.

$Pna2_1$ and tetragonal $P4/n$ space groups, respectively (Table S1). The $[Nd(CO_3)_4H_2O]^{5-}$ anion consists of four chelated CO_3^{2-} anions and a bonded H_2O molecule with a real C_1 symmetry in **1** and C_4 symmetry in **2** (Figure 1). For **1**, five guanidinium cations are arranged around the anion, forming a hydrogen-bonding network with two free water molecules in the crystal lattice (Figure S1), which makes the crystal stable in the air. For the lanthanide anion, the Nd(III) ion is in the plane of C1, C2, and C4 atoms (from carbonate) and the C3 atom is out of the plane with a mean deviation of 1.047 Å due to the steric hindrance. The related Nd-O lengths are in the range of 2.46–2.54 Å (Table S2). The coordinated water molecule is located on the quasi-C_4 axis with a longest Nd-O length (2.63 Å). For **2**, four guanidinium and one H_3O^+ cations behave as charge-balanced ions, arranged around the anion, forming the hydrogen bonding with other ten water molecules in the crystal lattice, which is similar to the reported complex $[C(NH_2)_3]_4[H_3O][Dy(CO_3)_4H_2O]\cdot13H_2O$ (Goff et al., 2010) as supported by thermogravimetric analysis (Figure S2). The crystal of **2** is unstable in the air at the room temperature but is quite stable below the ice point, which can be attributed to the large amount of lattice water molecules in the crystal lattice. In the lanthanide anion, the four C atoms from CO_3^{2-} are in the same plane and the Nd(III) ion is out of the plane with a mean deviation of 0.335 Å. The lengths of Nd-O bonds are in the range of 2.477–2.508 Å. The coordinated water molecule is located on the C_4 axis with a Nd-O length of 2.43 Å. More structural parameters are summarized in Table S2. If the carbonate anion is regarded as one coordination site, structure **2** could be considered to have the quasi-tetragonal pyramid symmetry with a C_4 axis.

Magnetic Properties

The direct-current (dc) magnetic susceptibilities of **1** and **2** were measured under 0.1 T in the temperature range of 1.8–300 K for **1** and 1.8–260 K for **2** (**2** is unstable above 260 K) (Figure S3). Notably, the $\chi_M T$ value is 1.50 $cm^3mol^{-1}K$ at 300 K for **1** (1.47 $cm^3mol^{-1}K$ at 260 K for **2**), lower than the expected value of one isolated Nd(III) ion (1.64 $cm^3mol^{-1}K$, for $J = 9/2$, $g_J = 8/11$) (Wada et al., 2017). Given that the crystal of **1** is stable, regular, and big enough, magnetization measurements at low temperatures were collected along three different orientations (a, b, and c) to determinate the susceptibility tensor (Figure S4). Through the single-crystal XRD analysis, the magnetization is 1.44, 1.54, and 0.59 $N\mu_B$ along the unit axes a, c, b, respectively. The magnetizations of a and c orientations increase quickly at low dc fields, slowly reaching to similar maximum values, whereas the magnetization of b orientation increases slowly in the whole field range, indicating that **1** is an "easy-plane" system. Treating the Nd(III) ion as an effective spin-1/2 ion, we could obtain the g-factor $g_x = 2.97(1)$, $g_y = 2.68(2)$, and $g_z = 1.23(1)$ by fitting the magnetizations with the Brillouin function (Darby, 1967). Considering the similarity of local symmetries between **1** and **2**, their magnetic anisotropy might be similar. In order to confirm the "easy-plane" anisotropy of **1** and **2**, HF-EPR measurements on polycrystalline samples were conducted at 4.2 K and in the frequency range of 60–253 GHz (Figure S5) (Wang et al., 2012; Nojiri and Ouyang, 2012). From the HF-EPR spectra, the relevant g-factors were obtained as $g_x = 3.00(2)$ and $g_y = 2.56(2)$ for **1** and $g_x = g_y = 2.79(2)$ for **2**, respectively, manifesting the "easy-plane" magnetic anisotropy for **1** and **2**. The resonance signals of g_z were not observed up to 22 T probably because the signals are too broad and hence weak due to the fast spin relaxations (Figure S6).

To study the origin of their magnetic properties, we performed the ab initio calculations (Karlstrom et al., 2003) for **1** and **2**. The results are summarized in Tables S6 and S7. The calculated magnetic axes of the ground state are shown in Figure S17. The calculated g values within CASSCF are $g_x = 3.10(5)$, $g_y = 3.01(7)$, and $g_z = 0.86(8)$ for **1** and $g_x = 3.12(1)$, $g_y = 3.07(1)$, and $g_z = 1.31(3)$ for **2**, which are in line with
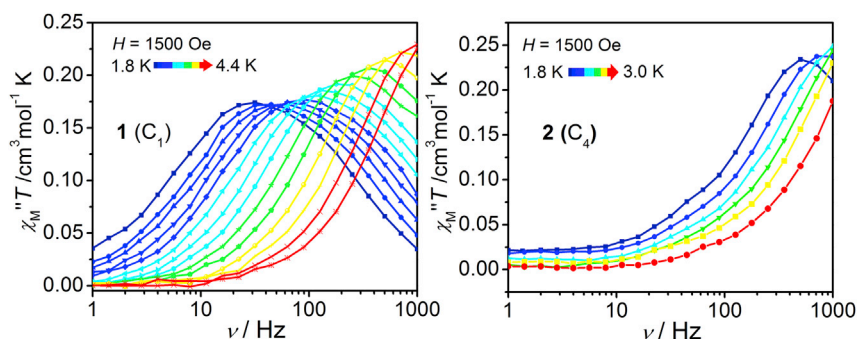
Figure 2. The Magnetic Relaxation of 1 and 2

Frequency dependence *ac* magnetic susceptibilities for **1** (left) and **2** (right) obtained under 1.5 kOe dc field. See also Figures S7–S14.

the aforementioned results from magnetization and HF-EPR measurements. The splitting of the two lowest Kramers doublets (KDs) for **1** was 99.5 cm^{-1} within CASSCF (128.6 cm^{-1} for **2**). Based on the observed *g* value of the lowest KDs, the ground state of **1** is mixed by several m_J states severely (Table S7), which may induce a large QTM between these states (proved by the high-field magnetization measurements as presented in Figure 3). The alternating-current (*ac*) magnetic susceptibility measurements were performed on **1** and **2** with polycrystalline samples at low temperatures. Without the external *dc* field, no out-of-phase susceptibility (χ_M'') signal appeared as predicted by the *ab initio* calculations (Figures S7 and S10). This could be ascribed to the strong quantum tunneling of magnetization (QTM) at zero *dc* field, which is common in easy-plane-type systems as observed in the high-field magnetization measurements (Figure 3). When a small external *dc* field was applied, obvious signals in the frequency dependence of χ_M'' were clearly observed in **1** and **2** (Figures S7 and S10), which might be due to the magnetic field-suppressed QTM or the strong phonon bottleneck effect. However, the maximum can only be observed in high frequency range under 1.5–2.0 kOe external *dc* field in **2**. This is the second time to discover that the light lanthanide complexes with the easy plane magnetic anisotropy can show slow spin relaxations (Table S8).

The temperature-dependent *ac* susceptibilities were measured under 1.5 kOe *dc* field (Figure 2, Figures S8 and S11). The relaxation times (τ) were obtained by fitting the Cole-Cole curves with the *CCFIT* program (Guo et al., 2011) (Figures S9 and S12). Complex **1** shows the slow magnetic relaxation in the temperature range of 1.8–4.4 K with relaxation times ranging from 4.39 ms at 1.8 K to 0.112 ms at 4.4 K. Complex **2** shows the slow magnetic relaxation in a lower temperature range (1.8–3.0 K), and the relaxation times (0.29–0.046 ms) are substantially lower than those of **1** (Figure S13). Complex **1** exhibits an exponential relationship for ln(τ) versus temperature, demonstrating that multiple relaxation mechanisms coexist in the relaxation process. By fitting the linear part in high temperature range (4.0–4.4 K for **1** and 2.4–3.0 K for **2**) with Arrhenius law $\tau = \tau_0 \exp(-U_{eff}/k_B T)$, thermal energy barriers were obtained as U_{eff} = 30.7 K with $\tau_0 = 1.05 \times 10^{-7}$ s for **1** and U_{eff} = 9.25 K with $\tau_0 = 2.09 \times 10^{-6}$ s for **2**. The barriers are much smaller than the calculated energy splitting between ground state and the first excited state (Table S6). As a result, Raman process might dominate in the whole relaxation process, which is common in the easy-plane systems. Fitting of the complete temperature range data to a sum of direct and Raman processes with Equation 1:

$$\tau^{-1} = AT + CT^n \qquad \text{(Equation 1)}$$

affords A = 125.89 K^{-1}s^{-1}, C = 0.89K$^{-6.08}$s^{-1}, and n = 6.08 for **1** (A = 0, C = 413.85 K$^{-3.63}$s^{-1}, and n = 3.63 for **2**). Interestingly, the exponent n of 3.63 for **2** approaches the value of 3 as predicted in the case that both the acoustic and optical vibrations are important in the spin dynamic process. For **1**, the n of 6.08 is close to 9, indicating that the acoustic vibration is dominated in the relaxation process (Abragam and Bleaney, 2012).

Phonon-bottleneck effect (PB effect) usually plays a crucial part in the slow magnetic relaxation of "easy plane" system (Zadrozny et al., 2012). For a phonon-supported relaxation process, the energy exchange occurs through two processes (Abragam and Bleaney, 2012): from spin to phonon (τ_{sp}) and from phonon to heat bath (τ_{pb}). So the relaxation time (τ) can be described in Equation 2:
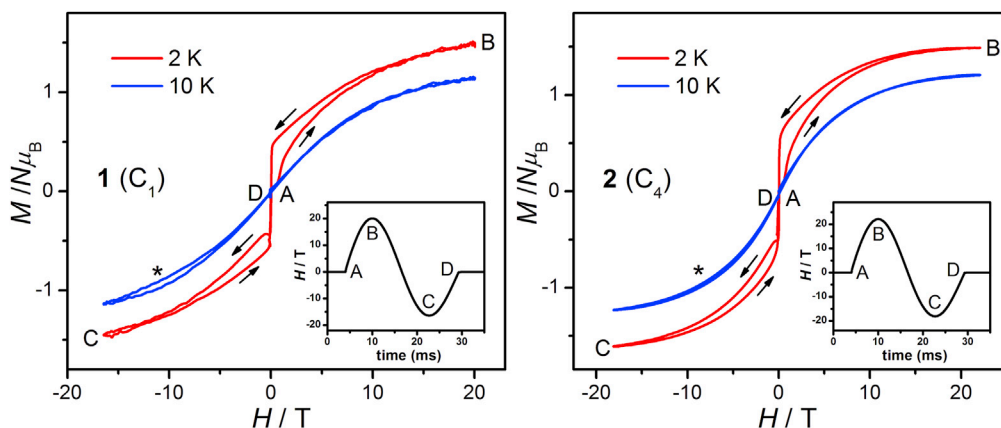
Figure 3. The Magnetic Hystersis Loop of 1 and 2

Magnetization versus pulsed magnetic field at 2 and 10 K for a powder sample of **1** (left) and **2** (right). The loop labeled by the asterisk is due to the experimental error when subtracting the background from the sample holder. Inset: Magnetic fields as a function of time. See also Figure S15.

$$\tau = \tau_{sp} + \frac{C_s}{C_p}\tau_{pb} \qquad \text{(Equation 2)}$$

where C_s and C_p represent the heat capacity of spins and phonons in crystals, respectively. For an SMM, the phonon in crystal is abundant, so the rate-determining step in the relaxation process is τ_{sp}. Hence, the relaxation time $\tau \approx \tau_{sp}$. The PB describes the situation that the number of spins is much larger than that of available phonons, in which the C_s/C_p can be in the order of 10^4–10^6. The theoretical PB relaxation time can be calculated through the following Equation 3:

$$\tau = \tau_{pb}\left(\frac{2\pi^2 v^3 N}{3\omega^2 \Delta\omega}\right) tanh^2(\hbar\omega / 2k_B T) \qquad \text{(Equation 3)}$$

where the τ_{ph} is the mean lifetime of lattice phonon, v is the averaged sound speed in the crystal, N is the spin carrier density, and ω is the resonant frequency of vibration modes. For complexes **1** and **2**, the vibration modes would be nearly the same due to the similar chemical composition. If the magnetization relaxation phenomena of **1** and **2** were supported by PB effect, the relaxation time τ would be sensitive to the spin density. From the crystal parameters, the spin density is $N_1 = 0.00144$ Nd/Å^3 in **1** and $N_2 = 0.00111$ Nd/Å^3 in **2**. Here, $N_1/N_2 > 1$, τ_1 would be longer than τ_2 at the same temperature, which is in agreement with the experimental results. On the other hand, in the PB-dominated relaxation process, the diffusion to the crystal boundary should be taken into consideration. The relaxation time, τ, is proportional consideration to the crystal size, L_1 or L_2. When the crystal is ground to a smaller size (Figure S14), the relaxation time would be short.

To justify the magnetization dynamic mechanism, *ac* measurements were tested on a ground powder sample of **1** at 2 K (Figures S7 and S14). After grinding, the size of the crystals became smaller, thus affecting only the single phonon process (Scott and Jeffries, 1962; Pedersen et al., 2015), so that Raman and Orbach processes would not be influenced. However, the maximum of χ_M'' for the ground powder sample shifts to the higher frequency range, indicating that the magnetic relaxation is sensitive to the low energy region of the phonon spectrum and/or the scattering of phonons on the crystal boundaries (Orendáč et al., 2016). Accordingly, the phonon bottleneck effect dominates the magnetic relaxation in the crystalline sample of **1**. Owing to the air instability, the *ac* susceptibility of the ground powder sample of **2** could not be explored.

The magnetic relaxation properties of **1** and **2** are further studied by the high-field magnetization measurements with a pulsed magnetic field (3000 T s^{-1} averagely, Figure 3) (Saito and Miyasata, 2001). At 2 K, by sweeping the pulsed field upwardly (A→B), the magnetization gradually increases to 1.5 Nμ_B at 20 T. In the down sweep (B→C), the magnetization decreases with a slower rate compared with upward sweeping, resulting in a pronounced hysteresis loop. A similar hysteresis loop is also observed in the negative field range. The hysteresis loops are due to the slow magnetic relaxations as observed in the *ac* susceptibility
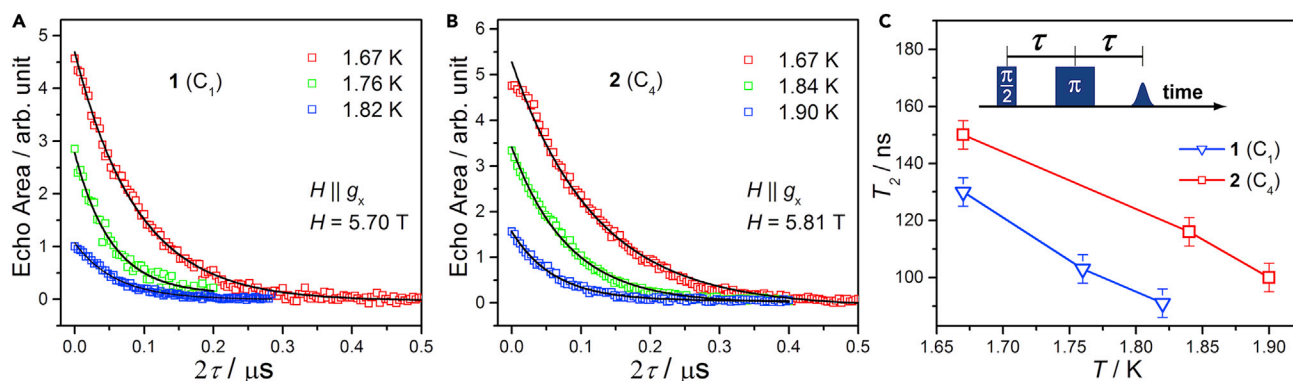
Figure 4. The Quantum Coherence of 1 and 2

(A and B) Echo signals as a function of 2τ at different temperatures and 240 GHz for **1** and **2**, respectively. Solid lines are the fits using a single exponential.

(C) Temperature dependence of the spin-spin relaxation time, T_2, for **1** and **2**.

studies. The hysteresis loops were also tested at the same temperature using Squid VSM in a low field sweep rate (100 Oe/s) (Figure S15). No open loop was observed in this situation, which means that both **1** and **2** are not the magnet above 2 K. Thus, it is the pulsed magnetic field that makes it possible to observe the slow relaxation behaviors of **1** and **2** considering the extremely fast scan rate. Under the high sweep rate, the spin relaxation is in an adiabatic process, which limits the energy exchange between the phonons of the crystals and the environment (Lopez et al., 2009; Schenker et al., 2005). As a result, the butterfly loops were observed, indicating the strong phonon bottleneck effect in these complexes, which is in accordance with the ac susceptibility measurements.

However, it seems that phonon bottleneck effect mechanism has not been valued by chemists, although it might play an important role in many complexes with slow magnetic relaxation behaviors. For some special systems, for example, $S = 1/2$ systems like Cu(II) (Boča et al., 2017), isotropic systems like Gd(III) (Holmberg et al., 2015), also show slow spin relaxation under low temperature with external field. To explain the special slow spin relaxation in those systems, chemists often attribute the relaxation behavior to Raman process without further discussions, which deserve further studies. This work opens a way to discuss the nature of the slow spin relaxation behaviors, especially to understand the origin of the slow magnetic relaxation behaviors in $S = 1/2$ and isotropic systems.

Quantum Coherence

Similar magnetization hysteresis loops were observed on a [Cu_3] spin triangle complex whose life time is long enough to be detected by the pulsed EPR, proving [Cu_3] complex a good candidate for qubit (Choi et al., 2012). So we studied the quantum decoherence properties of **1** and **2** on a 240 GHz pulsed EPR spectrometer at the National High Magnetic Field Laboratory, in Tallahassee, Florida, USA (van Tol et al., 2005; Morley et al., 2008). Measurements were done on single crystal samples, and the temperature dependence of quantum coherence time (T_2) has been collected with the magnetic field along the x axes considering the easy-plane magnetic anisotropy for **1** and **2**. The spin coherence time was measured by a Hahn echo sequence ($\pi/2 - \tau - \pi - \tau -$ echo), with the delay time τ varied during the measurements (Wernsdorfer et al., 2000; Schweiger and Jeschke, 2001). The widths of the pulses were tuned to maximize the echo signals and were typically between 100 and 150 ns. Figures 4A and 4B present the echo area as a function of 2τ at magnetic field 5.70 T for **1** and 5.81 T for **2** at different temperatures. The spin decoherence time T_2 was extracted from the decay rate of the echo area, which was well fit by a single exponent function (exp($-2\tau/T_2$)). Above 1.82 K for **1** (1.90 K for **2**), T_2 becomes too short to give spin echoes with the limited time resolution of the pulsed spectrometer. Taking into account the measurement temperature range (1.67–1.82 K for **1** and 1.67–1.90 K for **2**), it is clear that the echo decays are strongly temperature dependent (Figure 4C) and T_2 decreases from 130(5) ns at 1.67 K to 91(5) ns at 1.82 K for **1** (150(5) ns at 1.67 K to 100(5) ns at 1.90 K for **2**).

The spin decoherence time of **1** and **2** is close to that of the first single crystal SMM qubit [Fe_8] (Takahashi et al., 2009). At the low temperature of 2 K and the strong magnetic fields ($H = 5.70$ T for **1** and 5.81 T for **2**),
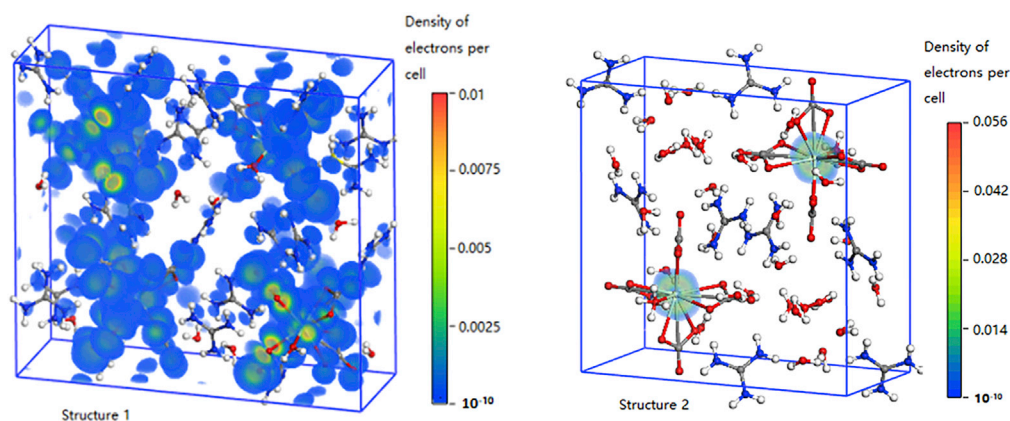
Figure 5. The Spatial Distributions of the Spin States of 1 and 2

The spatial distributions of the spin states at the Fermi level in Nd atom and its four ligands for both **1** and **2**. Green balls are for Nd atoms, red for O, blue for N, gray for C, and white for H. See also Figure S18.

more than 99% of Nd spins are polarized to the lowest lying spin state, which suppresses the spin flip-flop process significantly. That is the most important reason why the echo can be observed under concentrated samples. The strong temperature dependence of T_2 can be ascribed to spin bath (Takahashi et al., 2008) fluctuation dominated by an energy-conserving spin flip-flop process. To our knowledge, many factors like hyperfine coupling (Wernsdorfer et al., 2000), the distance of spin carriers, and so on, influence the decoherence path. Considering that more H_2O molecules are around the $[Nd(CO_3)_4H_2O]^{5-}$ ion in **2** than in **1**, one would expect faster spin decoherence in **2**. However, the opposite was observed in our study, to put it more clearly, the spin decoherence time of **2** is longer than **1** at the same temperatures. According to the conclusion of Takahashi (Takahashi et al., 2011), the effect of nuclear spin and magnetic exciton on decoherence is much smaller than the phonon effect under high magnetic field and ultralow temperature. Here, the $[Nd(CO_3)_4H_2O]^{5-}$ cluster in **2** is C_4 symmetric, whereas **1** is C_1 symmetric. Therefore, the phonon spectrum of **1** would be more complicated than that of **2** because the local vibration modes in **1** are more than in **2**. The more complicated phonon freedom in **1** would increase the spin decoherence probability. From this point of view, the spin decoherence time of **2** with the high local symmetry should be longer at the same temperature and magnetic field.

The First Principle Calculations

To investigate the origin of the difference in the spin relaxation rate between **1** and **2**, we perform the first principle calculations for the eigenstates and eigenvalues of these two samples (Mendeley Data). It is found that, for both **1** and **2**, the magnetic moments mainly come from the f states of Nd atoms at the top of the valence band (Figure S18). The corresponding eigenstates, however, are very different for **1** and **2**. For **1**, the eigenstate at the top of the valence band is extended to both the Nd atom and the nearby four CO_3^{2-} ligands, but for **2**, this eigenstate is localized within the Nd atom (Figure 5). This can be well understood from symmetry point of view. The Nd-O-C structure in **2** is C_4 symmetric, so that the hopping channels of electrons between the Nd atom and its four nearby CO_3^{2-} ligands can be suppressed most by the destructive interference, whereas such a suppression of hoppings does not happen in **1** as it has C_1 symmetry. The different symmetry can lead to remarkable difference in the spin relaxation rate between **1** and **2**, because the spin-orbit interaction (SOI) together with phonons or charge fluctuations exert considerable influence in the spin relaxation processes (Khaetskii and Nazarov, 2001), and the hoppings between the Nd atom and its CO_3^{2-} ligands contribute largely to the orbital motion of electrons in the spin state both in structures **1** and **2**. In this spin relaxation channel, the SOI provides the spin flip mechanism during the electron orbital motion, whereas the phonons or charge fluctuations cause the dissipation. The relaxation rate of the spin-flip process is proportional to the square of the absolute value of the spin-flip matrix element (Khaetskii and Nazarov, 2001), i.e. $\Gamma = \frac{1}{T_1} \propto |(H^{\uparrow\downarrow})|^2$

In the present case, the main part of the orbital motion is due to the hopping processes between the Nd atoms and their ligands. Through the SOI, the spin-flip occurs during these hopping processes. Based on

the above-mentioned results of the first principle calculations, the hopping processes between the Nd atom and its ligands are strongly suppressed in structure **2** due to the C_4 symmetry, whereas in **1** such suppression does not happen. Therefore, in **2** the spin-flip processes due to the SOI are also suppressed, leading to the much longer spin-flip relaxation time in structure **2** compared with structure 1, $T_1(\textbf{2}) > T_1(\textbf{1})$. At the same time, $T_2 \leq 2T_1$ (Golovach et al., 2004) is still valid for both structures **1** and **2**. It is also shown that, for localized spin states, such as the case in the quantum dots, one has $T_2 = 2T_1$ for all SOI mechanisms in leading order of the electron-phonon interaction (Golovach et al., 2004). The localization of the spin state in structure **2** is very similar to the case in the quantum dots, in which $T_2(\textbf{2}) = 2T_1(\textbf{2})$ holds. Hence $T_2(\textbf{2}) > T_2(\textbf{1})$ is reasonable as observed in our experiments.

CONCLUSIONS

In summary, typical magnetic relaxation behaviors have been observed for two mononuclear Nd(III) complexes **1** and **2** with strong easy-plane magnetic anisotropy due to the strong phonon bottleneck effect. The spin decoherence studies reveal that the higher symmetry results in longer decoherence times, which is explained by the first principle calculations. Furthermore, consistent with the work of [GdW$_{10}$] reported by Coronado (Martinez-Perez et al., 2012), we believe that the easy-plane magnetic anisotropy and high symmetry are extremely important factors to enhance spin decoherence time of molecular spin carriers. Further studies of spin decoherence in other lanthanide complexes are in progress in our laboratory.

Limitations of the Study

This work demonstrates that the symmetry is an important factor to develop potential qubits with the improved performance and the higher symmetry results in longer decoherence times. This discovery provides a specific design criteria to develop potential qubits with improved performances. However, the decoherence times of complexes **1** and **2** are too short to application. And we need more couples of samples and more accurate physical model to understand the deep influence of symmetry in quantum coherence.

METHODS

All methods can be found in the accompanying Transparent Methods supplemental file.

DATA AND CODE AVAILABILITY

Crystallographic data have been deposited in the Cambridge Crystallographic Data Centre under the accession numbers CCDC: 1546890 and 1860144.

SUPPLEMENTAL INFORMATION

Supplemental Information can be found online at https://doi.org/10.1016/j.isci.2020.100926.

AUTHOR CONTRIBUTIONS

Investigation, J.L., Y.S., and Z.W.; Synthetic studies, J.L.; Crystallographic studies, F.Y.; HF-EPR experiments, L.Y., Z.-W.O., and Z.W.; SQUID experiments, J. L.; Pulsed magnetization, Z.-C.X.; Quantum coherence, J.L., Z.W., and J.V.T.; Computational experiments, Y.-Q.Z., S.-J.X., and X.-L.W.; Writing – Original Draft, J.L., Z.W., X.-L.W., and Y.S.; Writing – Review & Editing, Z.W. and Y.S.

DECLARATION OF INTERESTS

The authors declare no competing interests.

REFERENCES

Abragam, A., and Bleaney, B. (2012). Electron Paramagnetic Resonance of Transition Ions (Oxford University Press).

Aguila, D., Barrios, L.A., Velasco, V., Roubeau, O., Repolles, A., Alonso, P.J., Sese, J., Teat, S.J., Luis, F., and Aromí, G. (2014). Heterodimetallic [LnLn'] lanthanide complexes: toward a chemical design of two-qubit molecular spin quantum gates. J. Am. Chem. Soc. 136, 14215–14222.

Atzori, M., Morra, E., Tesi, L., Albino, A., Chiesa, M., Sorace, L., and Sessoli, R. (2016a). Quantum coherence times enhancement in vanadium(IV)-based potential molecular qubits: the key role of the vanadyl moiety. J. Am. Chem. Soc. 138, 11234–11244.

Atzori, M., Tesi, L., Benci, S., Lunghi, A., Righini, R., Taschin, A., Torre, R., Sorace, L., and Sessoli, R. (2017). Spin dynamics and low energy vibrations: insights from vanadyl-based potential molecular qubits. J. Am. Chem. Soc. 139, 4338–4341.

Atzori, M., Tesi, L., Morra, E., Chiesa, M., Sorace, L., and Sessoli, R. (2016b). Room-temperature quantum coherence and rabi oscillations in vanadyl phthalocyanine: toward multifunctional molecular spin qubits. J. Am. Chem. Soc. 138, 2154–2157.

Boča, R., Rajnák, C., Titiš, J., and Valigura, D. (2017). Field supported slow magnetic relaxation in a mononuclear Cu(II) complex. Inorg. Chem. 56, 1478.

Choi, K.Y., Wang, Z., Nojiri, H., van Tol, J., Kumar, P., Lemmens, P., Bassil, B.S., Kortz, U., and Dalal, N.S. (2012). Coherent manipulation of electron spins in the {Cu3} spin triangle complex impregnated in nanoporous silicon. Phys. Rev. Lett. 108, 067206.

Darby, M.I. (1967). Tables of the Brillouin function and of the related function for the spontaneous magnetization. Br. J. Appl. Phys. 18, 1415–1417.

Ding, Y.-S., Chilton, N.F., Winpenny, R.E.P., and Zheng, Y.-Z. (2016). On approaching the limit of molecular magnetic anisotropy: a near-perfect pentagonal bipyramidal dysprosium(III) single-molecule magnet. Angew. Chem. Int. Ed. 55, 16071–16074.

Fataftah, M.S., Zadrozny, J.M., Coste, S.C., Graham, M.J., Rogers, D.M., and Freedman, D.E. (2016). Employing forbidden transitions as qubits in a nuclear spin-free chromium complex. J. Am. Chem. Soc. 138, 1344–1348.

Goff, G.S., Cisneros, M.R., Kluk, C., Williamson, K., Scott, B., Reilly, S., and Runde, W. (2010). Synthesis and structural characterization of molecular Dy(III) and Er(III) tetra-carbonates. Inorg. Chem. 49, 6558–6564.

Golovach, V.N., Khaetskii, A., and Loss, D. (2004). Phonon-induced decay of the electron spin in quantum dots. Phys. Rev. Lett. 93, 016601.

Graham, M.J., Zadrozny, J.M., Shiddiq, M., Anderson, J.S., Fataftah, M.S., Hill, S., and Freedman, D.E. (2014). Influence of electronic spin and spin-orbit coupling on decoherence in mononuclear transition metal complexes. J. Am. Chem. Soc. 136, 7623–7626.

Guo, Y.N., Xu, G.F., Guo, Y., and Tang, J. (2011). Relaxation dynamics of dysprosium(III) single molecule magnets. Dalton Trans. 40, 9953–9963.

Holmberg, R.J., Anh Ho, L.T., Ungur, L., Korobkov, I., Chilbotaru, L.F., and Murugesu, M. (2015). Observation of unusual slow-relaxation of the magnetization in a Gd-EDTA chelate. Dalton Trans. 44, 20321.

Karlstrom, G., Lindh, R., Malmqvist, P.A., Roos, B.O., Ryde, U., Veryazov, V., Widmark, P.O., Cossi, M., Schimmelpfennig, B., Neogrady, P., and Seijo, L. (2003). MOLCAS: a program package for computational chemistry. Comput. Mater. Sci. 28, 222–239.

Khaetskii, A.V., and Nazarov, Y.V. (2001). Spin-flip transitions between Zeeman sublevels in semiconductor quantum dots. Phys. Rev. B 64, 125316.

Leuenberger, M.N., and Loss, D. (2001). Quantum computing in molecular magnets. Nature 410, 789–793.

Lopez, N., Prosvirin, A.V., Zhao, H., Wernsdorfer, W., and Dunbar, K.R. (2009). Heterospin single-molecule magnets based on Terbium ions and TCNQF4 radicals: interplay between single-molecule magnet and phonon bottleneck phenomena investigated by dilution studies. Chem. Eur. J. 15, 11390–11400.

Martinez-Perez, M.J., Cardona-Serra, S., Schlegel, C., Moro, F., Alonso, P.J., Prima-Garcia, H., Clemente-Juan, J.M., Evangelisti, M., Gaita-Arino, A., Sese, J., et al. (2012). Gd-based single-ion magnets with tunable magnetic anisotropy: molecular design of spin qubits. Phys. Rev. Lett. 108, 247213.

Morley, G.W., Brunel, L.-C., and van Tol, J. (2008). A multifrequency high-field pulsed electron paramagnetic resonance/electron-nuclear double resonance spectrometer. Rev. Sci. Instrum. 79, 064703.

Nojiri, H., and Ouyang, Z.W. (2012). THz Electron Spin Resonance on Nanomagnets. Terahertz Sci. Technol. 5, 1–10.

Orendáč, M., Tibenská, K., Strečka, J., Čisárová, J., Tkáč, V., Orendáčová, A., Čižmár, E., Prokleška, J., and Sechovský, V. (2016). Cross-tunneling and phonon bottleneck effects in the relaxation phenomena of XY pyrochlore antiferromagnet Er2Ti2O7. Phys. Rev. B 93, 024410.

Pedersen, K.S., Dreiser, J., Weihe, H., Sibille, R., Johannesen, H.V., Sørensen, M.A., Nielsen, B.E., Sigrist, M., Mutka, H., Rols, S., et al. (2015). Design

of single-molecule magnets: insufficiency of the anisotropy barrier as the sole criterion. Inorg. Chem. 54, 7600–7606.

Pedersen, K.S., Ariciu, A.-M., McAdams, S., Weihe, H., Bendix, J., Tuna, F., and Piligkos, S. (2016). Toward molecular 4f single-ion magnet qubits. J. Am. Chem. Soc. 138, 5801–5804.

Runde, W., Neu, M.P., Pelt, C.V., and Scott, B.L. (2000). Single crystal and solution complex structure of Nd(CO3)4^5-. The first characterization of a mononuclear lanthanide(III) carbonato complex. Inorg. Chem. 39, 1050–1051.

Saito, K., and Miyasata, S. (2001). Magnetic foehn effect in adiabatic transition. J. Phys. Soc. Jpn. 70, 3385–3390.

Schenker, R., Leuenberger, M.N., Chaboussant, G., Loss, D., and Güdel, H. (2005). Phonon bottleneck effect leads to observation of quantum tunneling of the magnetization and butterfly hysteresis loops in (Et4N)3Fe2F9. Phys. Rev. B 72, 184403.

Schweiger, A., and Jeschke, G. (2001). Principles of Pulse Electron Paramagnetic Resonance (Oxford Univeristy Press).

Scott, P.L., and Jeffries, C.D. (1962). Spin-lattice relaxation in some rare-earth salts at Helium temperatures: observation of the phonon bottleneck. Phys. Rev. 127, 32–51.

Sessoli, R., Gatteschi, D., Caneschi, A., and Novak, M.A. (1993). Magnetic bistability in a metal-ion cluster. Nature 365, 141–143.

Shiddiq, M., Komijani, D., Duan, Y., Gaita-Ariño, A., Coronado, E., and Hill, S. (2016). Enhancing coherence in molecular spin qubits via atomic clock transitions. Nature 531, 348–351.

Takahashi, S., Hanson, R., van Tol, J., Sherwin, M.S., and Awschalom, D.D. (2008). Quenching spin decoherence in diamond through spin bath polarization. Phys. Rev. Lett. 101, 047601.

Takahashi, S., van Tol, J., Beedle, C.C., Hendrickson, D.N., Brunel, L.C., and Sherwin, M.S. (2009). Coherent manipulation and decoherence of S = 10 single-molecule magnets. Phys. Rev. Lett. 102, 08760.

Takahashi, S., Tupitsyn, I.S., van Tol, J., Beedle, C.C., Hendrickson, D.N., and Stamp, P.C.E. (2011). Decoherence in crystals of quantum molecular magnets. Nature 476, 76–79.

Tesi, L., Lucaccini, E., Cimatti, I., Perfetti, M., Mannini, M., Atzori, M., Morra, E., Chiesa, M., Caneschi, A., Sorace, L., and Sessoli, R. (2016). Quantum coherence in a processable vanadyl complex: new tools for the search of molecular spin qubits. Chem. Sci. 7, 2074–2083.

Thiele, S., Balestro, F., Ballou, R., Klyatskaya, S., Ruben, M., and Wernsdorfer, W. (2014).

Electrically driven nuclear spin resonance in single-molecule magnets. Science *344*, 1135.

van Tol, J., Brunel, L.-C., and Wylde, R.J. (2005). A quasioptical transient electron spin resonance spectrometer operating at 120 and 240 GHz. Rev. Sci. Instrum. *76*, 074101.

Wada, H., Ooka, S., Yamamura, T., and Kajiwara, T. (2017). Light lanthanide complexes with crown ether and its Aza derivative which show slow magnetic relaxation behaviors. Inorg. Chem. *56*, 147–155.

Wang, Z., Datta, S., Papatriantafyllopoulou, C., Christou, G., Dalal, N.S., van Tol, J., and Hill, S.

(2011). Spin decoherence in an iron-based magnetic cluster. Polyhedron *30*, 3193–3196.

Wang, S.L., Li, L., Ouyang, Z.W., Xia, Z.C., Xia, N.M., Peng, T., and Zhang, K.B. (2012). Development of high-magnetic-field, high-frequency electronic spin resonance system. Acta Phys. Sin. *61*, 107601.

Wernsdorfer, W., Caneschi, A., Sessoli, R., Gatteschi, D., Cornia, A., Villar, V., and Paulsen, C. (2000). Effects of nuclear spins on the quantum relaxation of the magnetization for the molecular nanomagnet Fe8. Phys. Rev. Lett. *84*, 2965.

Yu, C.-J., Graham, M.J., Zadrozny, J.M., Niklas, J., Krzyaniak, M.D., Wasielewski, M.R., Poluektov, O.G., and Freedman, D.E. (2016). Long coherence times in nuclear spin-free vanadyl qubits. J. Am. Chem. Soc. *138*, 14678–14685.

Zadrozny, J.M., Liu, J., Piro, N.A., Chang, C.J., Hill, S., and Long, J.R. (2012). Slow magnetic relaxation in a pseudotetrahedral cobalt(II) complex with easy-plane anisotropy. Chem. Commun. (Camb.) *48*, 3927–3929.

Zadrozny, J.M., Gallagher, A.T., Harris, T.D., and Freedman, D.E. (2017). A porous Array of clock qubits. J. Am. Chem. Soc. *139*, 7089–7094.
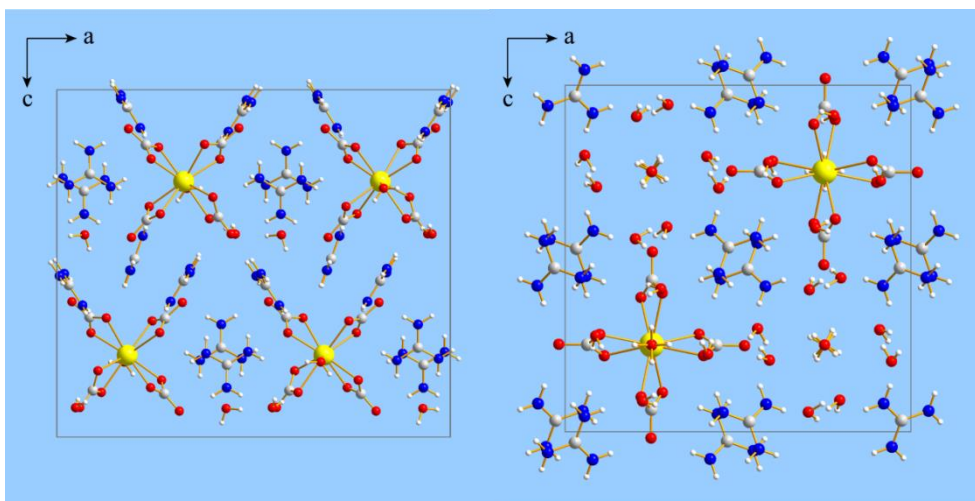
Supplemental Information

Controlling Electron Spin Decoherence

in Nd-based Complexes via Symmetry Selection

Jing Li, Lei Yin, Shi-Jie Xiong, Xing-Long Wu, Fei Yu, Zhong-Wen Ouyang, Zheng-Cai Xia, Yi-Quan Zhang, Johan van Tol, You Song, and Zhenxing Wang

Supporting Information

Supplemental Figures

Figure S1. Packing diagrams of **1**(left) and **2** (right) in the crystal structure viewed along the *b* axis. Color codes: Nd, yellow; O, red; N, blue; C, gray; H, white. Related to Figure 1.
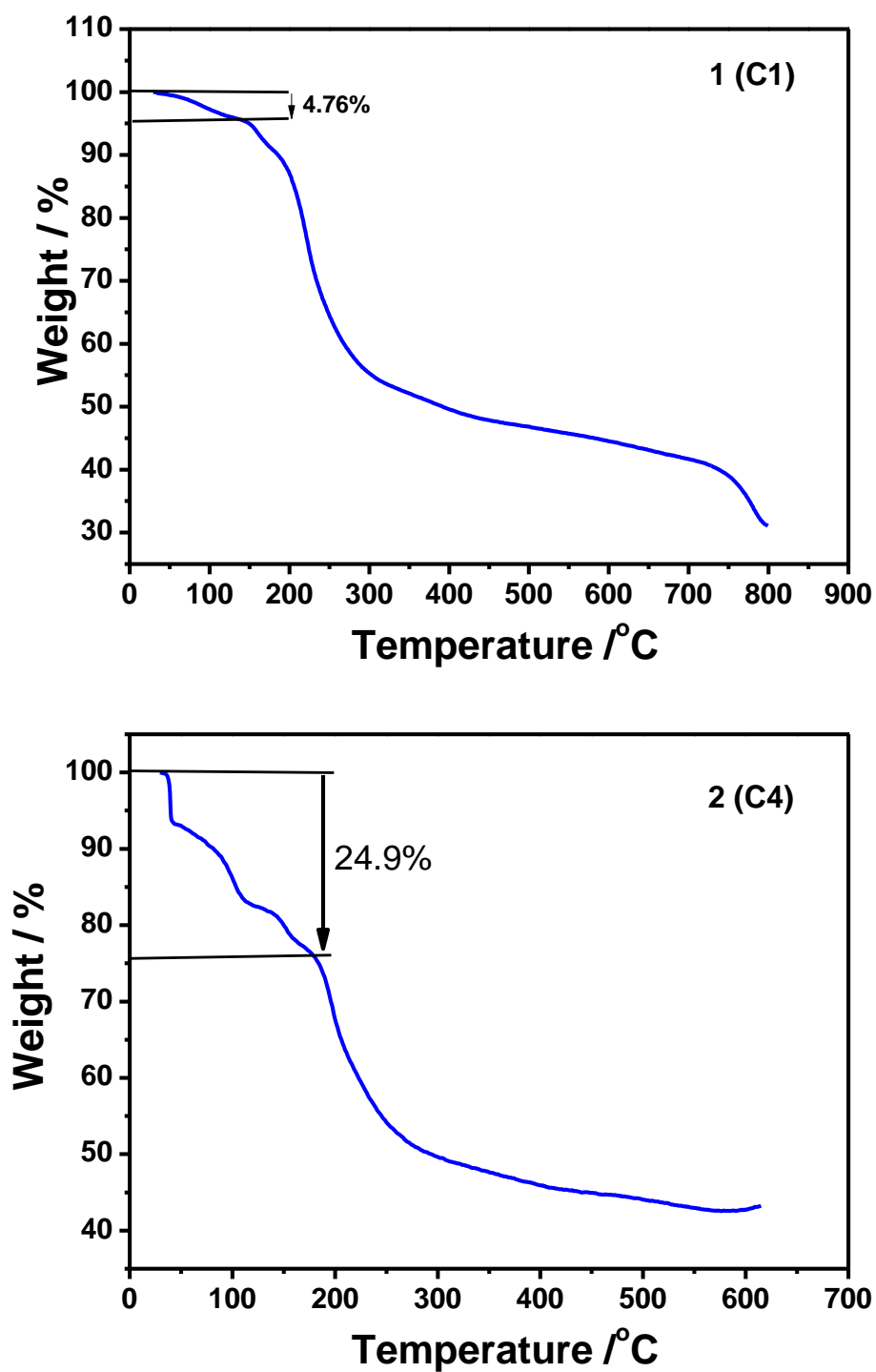
Figure S2. Thermogravimetric analysis of **1** (top) and **2** (bottom) in N$_2$. The ramp rates were 10 °C min^{-1} for **1** from 25 to 800 °C and 5 °C min^{-1} for **2** from 25 to 615 °C. Related to Figure 1.
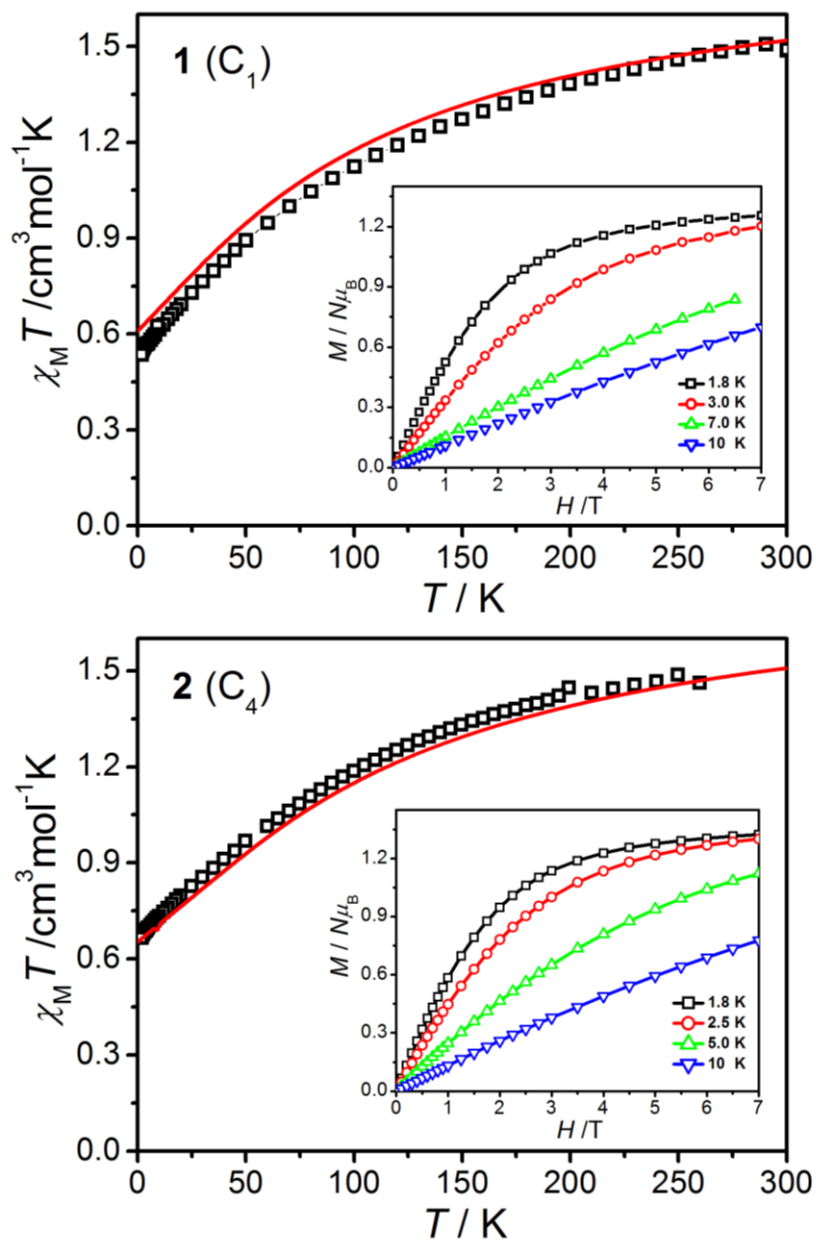
Figure S3. Temperature dependence of $\chi_M T$ under 1 kOe applied *dc* field at 1.8–300 K for a polycrystalline sample of **1**(top) and **2** (bottom) by MPMS-XL7. The solid line represents the calculated magnetic susceptibilities with CASSCF. Inset: Field dependence of magnetization under low temperature. Related to Figure 2.
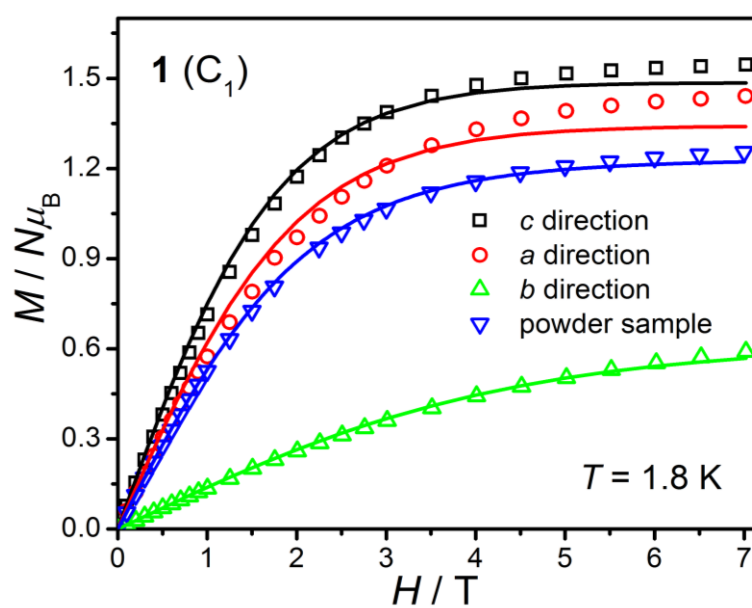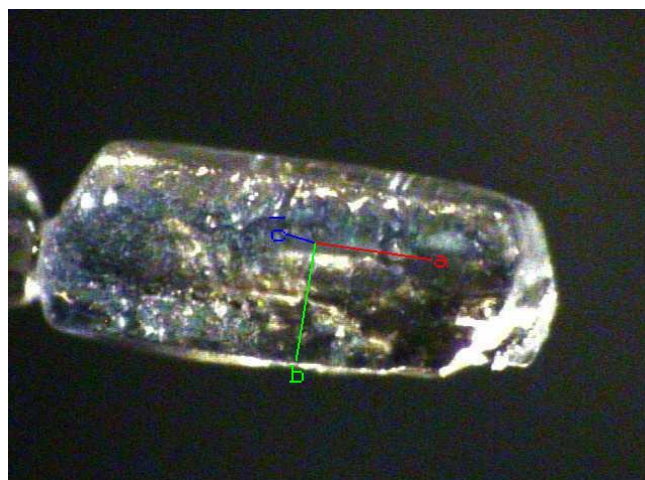
Figure S4. Top: The cell parameter *a*, *b*, *c* in the crystal from the single-crystal XRD analysis. Static magnetization data of a single crystal sample of **1**. Right: Low temperature magnetization *vs H*. the solid lines are best fits. Related to Figure 2.
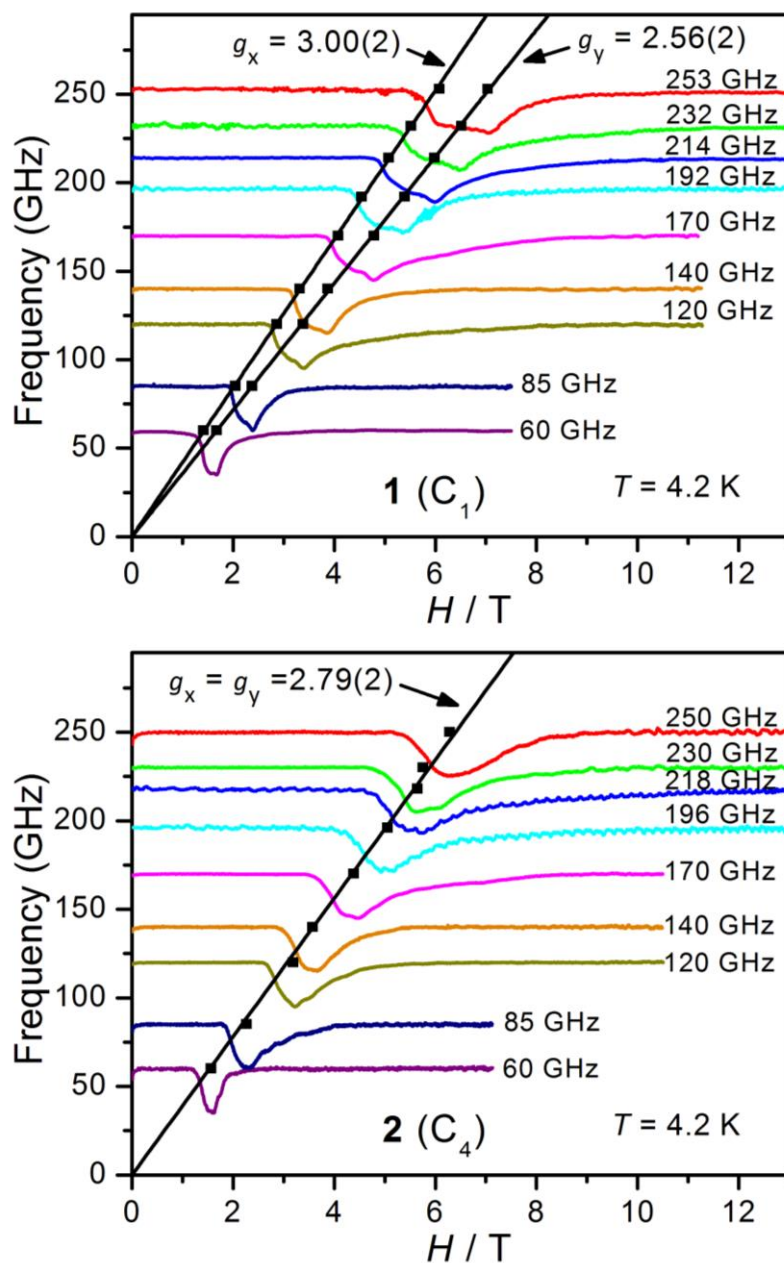
Figure S5. Variable-frequency EPR spectra collected on powder samples of **1** (top) and **2** (bottom) under 4.2 K. Solid lines are simulations of the frequency dependence of the peak positions employing the parameters given in the text. Related to Figure 2.

1 (C$_1$)

2 (C$_4$)

ν = 60 GHz
T = 4.2 K

H / T
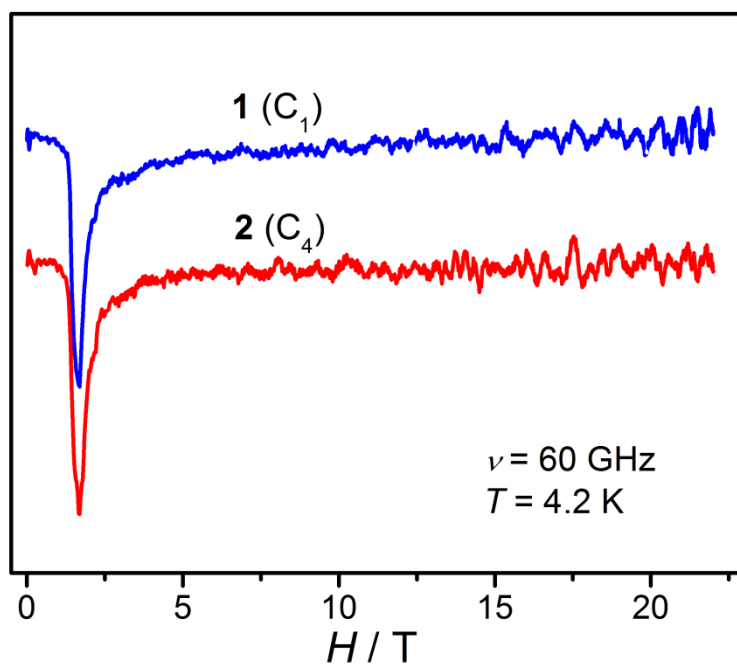
Figure S6. HF-EPR spectrum for a polycrystalline sample of **1** at 60 GHz and 4.2 K. Related to Figure 2.
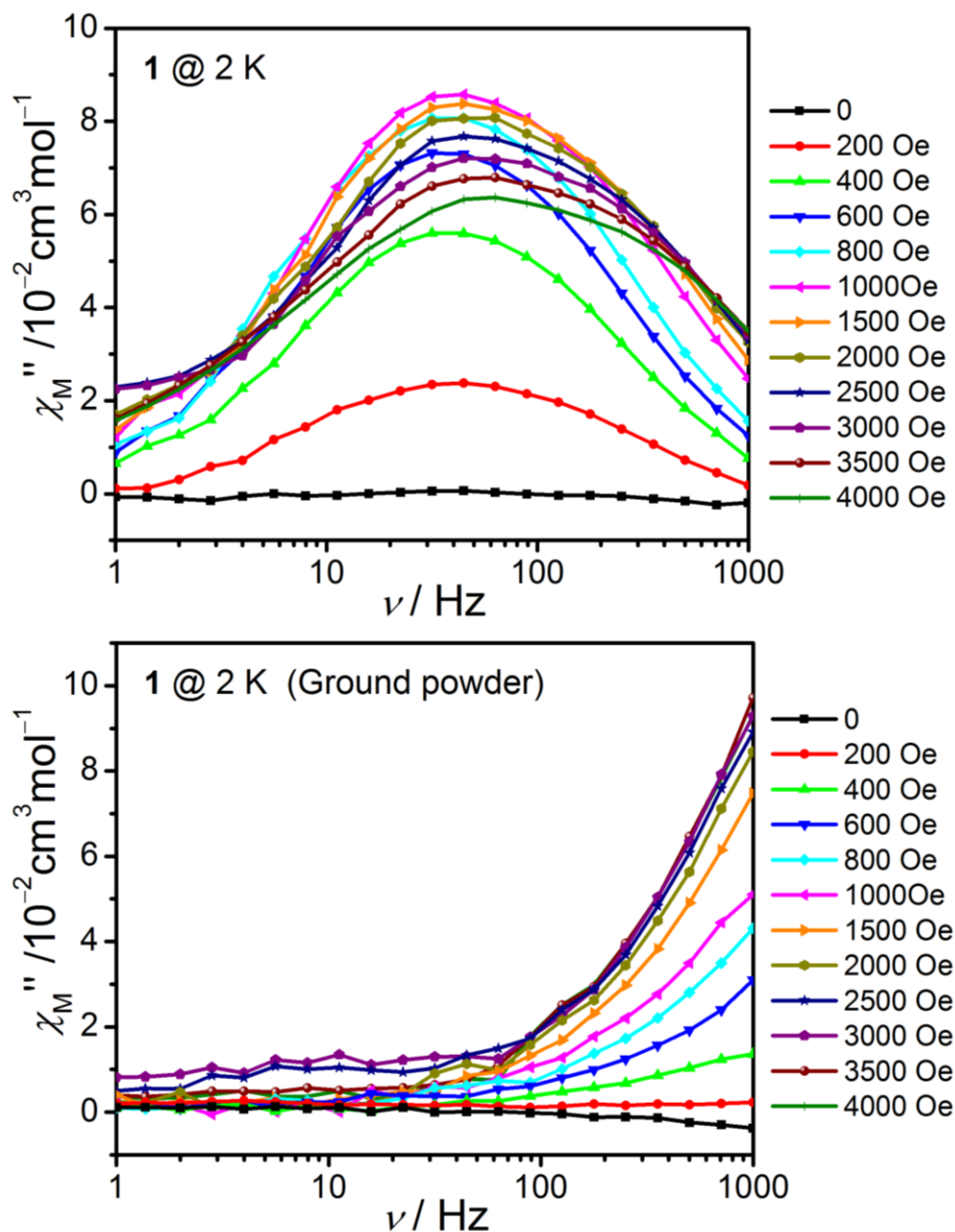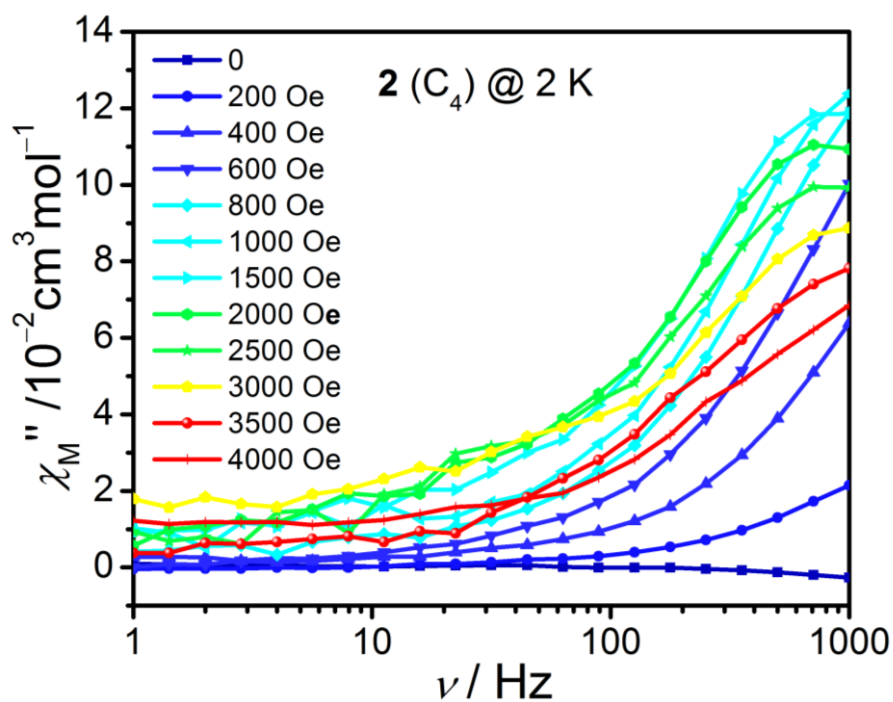
Figure S7. Variable-frequency out-of-phase χ_M'' components of the *ac* magnetic susceptibilities collected for a polycrystalline (top) and a ground (bottom) powder samples of **1** at 2.0 K under different applied *dc* fields. Related to Figure 2.
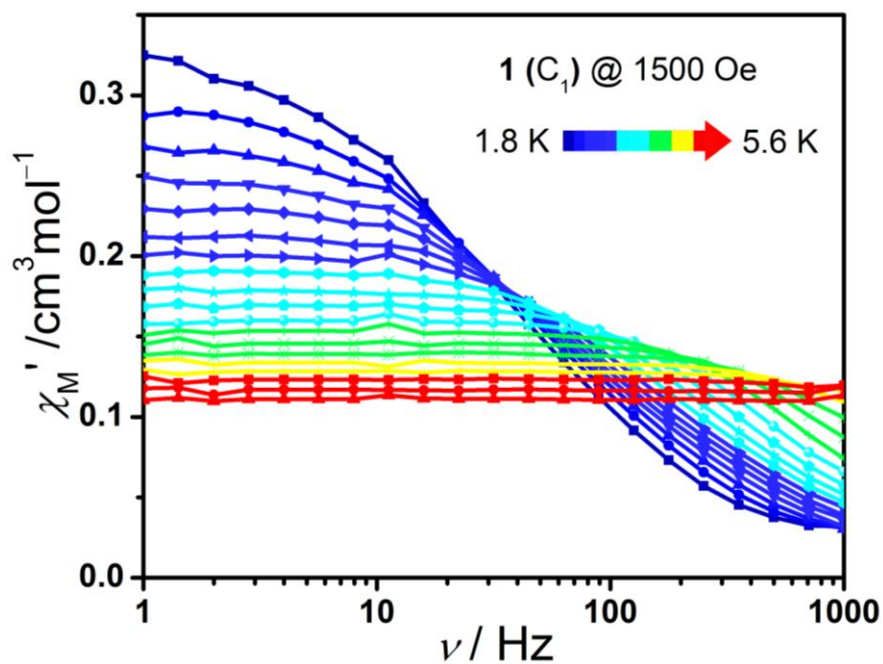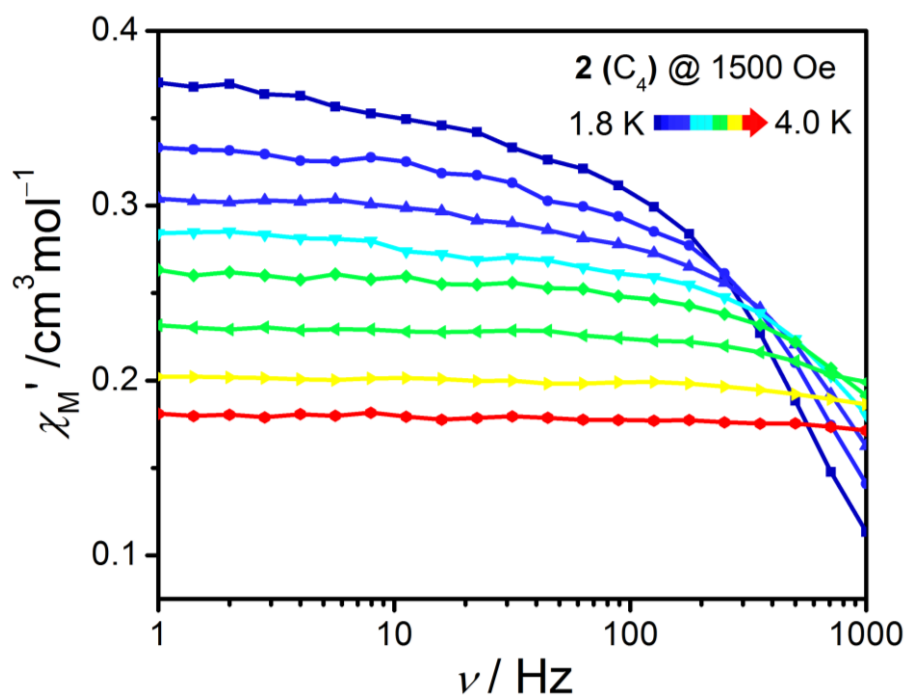
Figure S8. Frequency dependence of the in-phase (χ_M') *ac* susceptibilities under 1500 Oe *dc* field (1–999 Hz, by MPMS Squid VSM) at indicated temperatures for **1**. Related to Figure 2
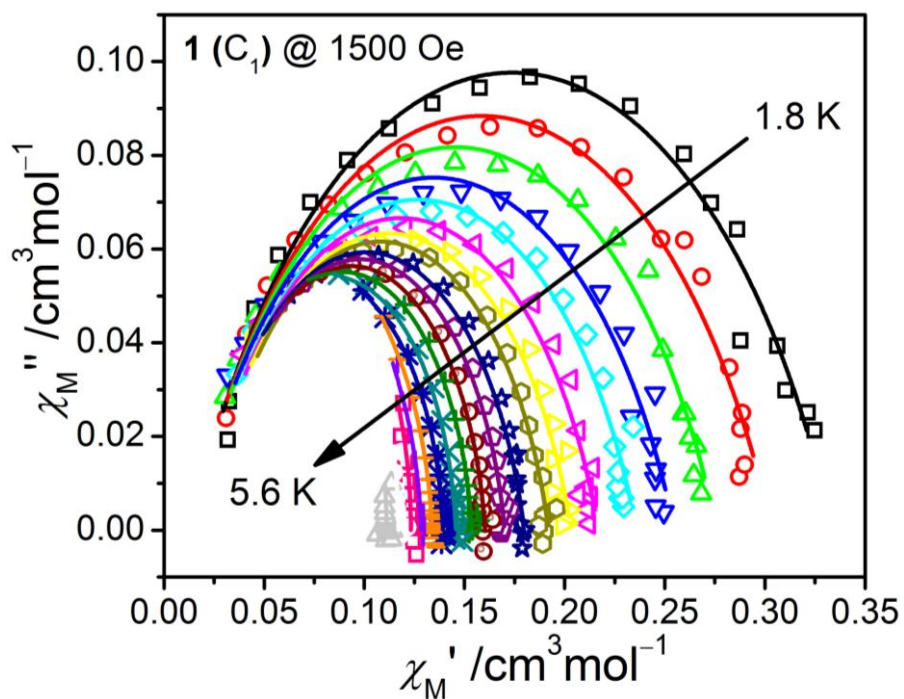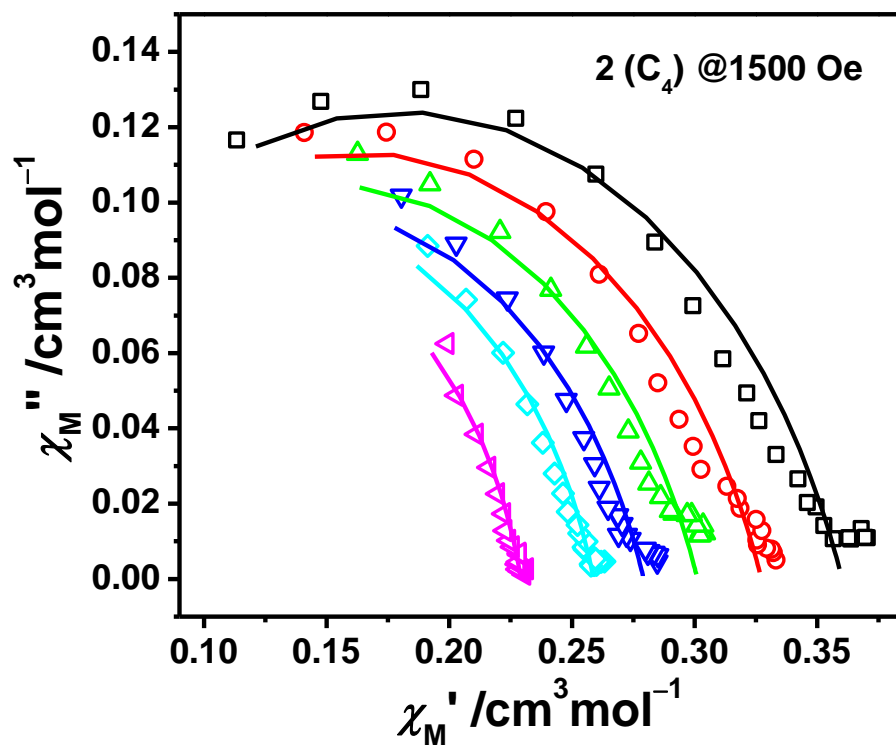

Figure S9. Variable temperature Cole-Cole plots under 1500 Oe *dc* field at different temperatures for complex **1**. Related to Figure 2

Figure S10. Variable-frequency out-of-phase χ_M'' components of the *ac* magnetic susceptibility collected for a polycrystalline sample of **2** at 2.0 K under different applied *dc* fields. Related to Figure 2.

Figure S11. Frequency dependence of the in-phase (χ_M') *ac* susceptibilities under 1500 Oe *dc* field (1–999 Hz, by MPMS Squid VSM) at indicated temperatures for **2**. Related to Figure 2.

Figure S12. Variable temperature Cole-Cole plots under 1500 Oe *dc* field at indicated temperatures for complex **2**. Related to Figure 2.
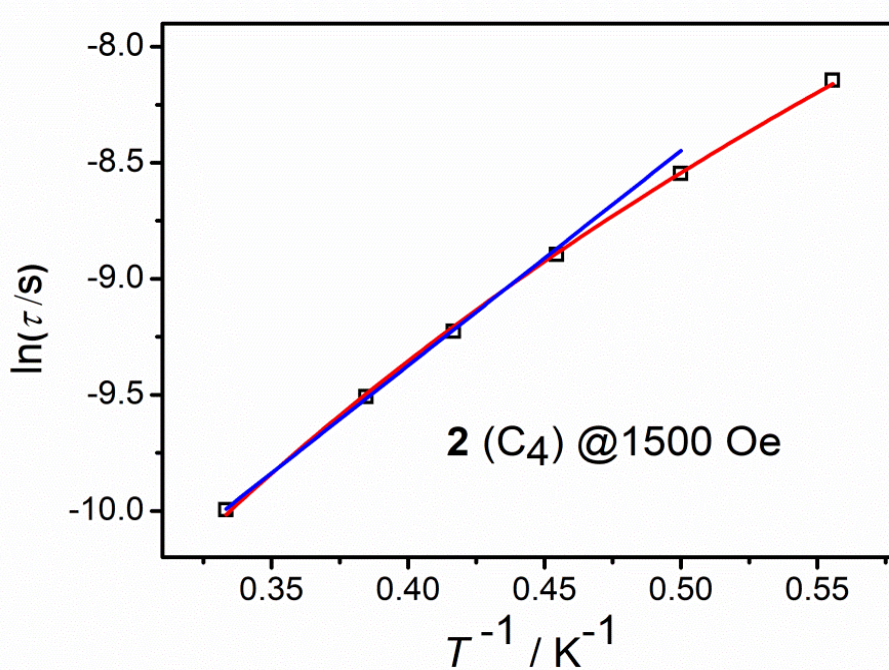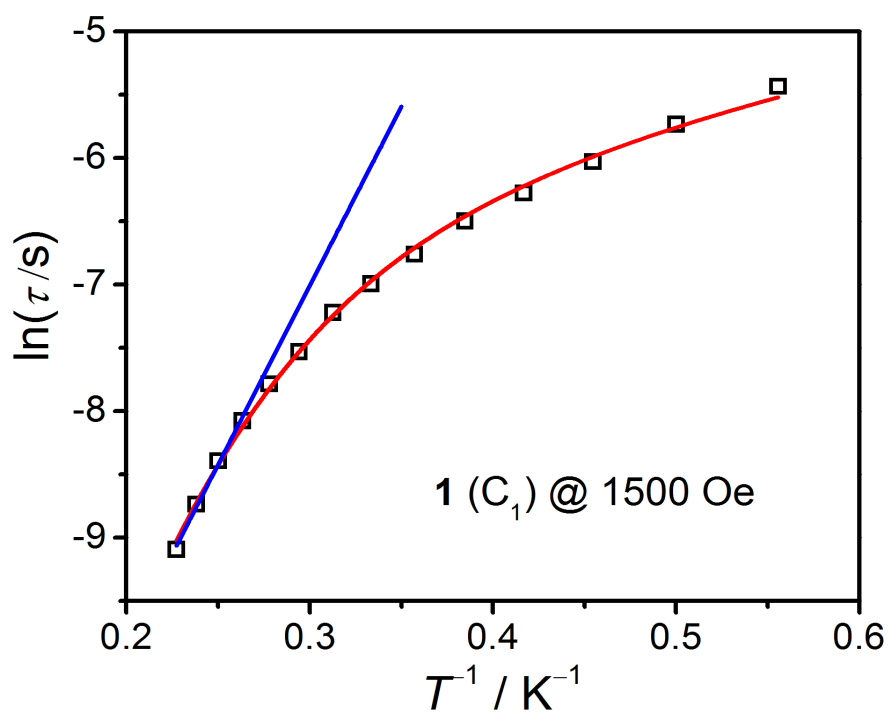
Figure S13. Arrhenius plot of ln(τ) as a function of T^{-1}. The blue solid lines are fitting results with Arrhenius law $\tau = \tau_0 \exp(U_{\text{eff}}/k_B T)$; red solid lines are fitting results with $\tau^{-1} = AT + CT^n$. Related to Figure 2.
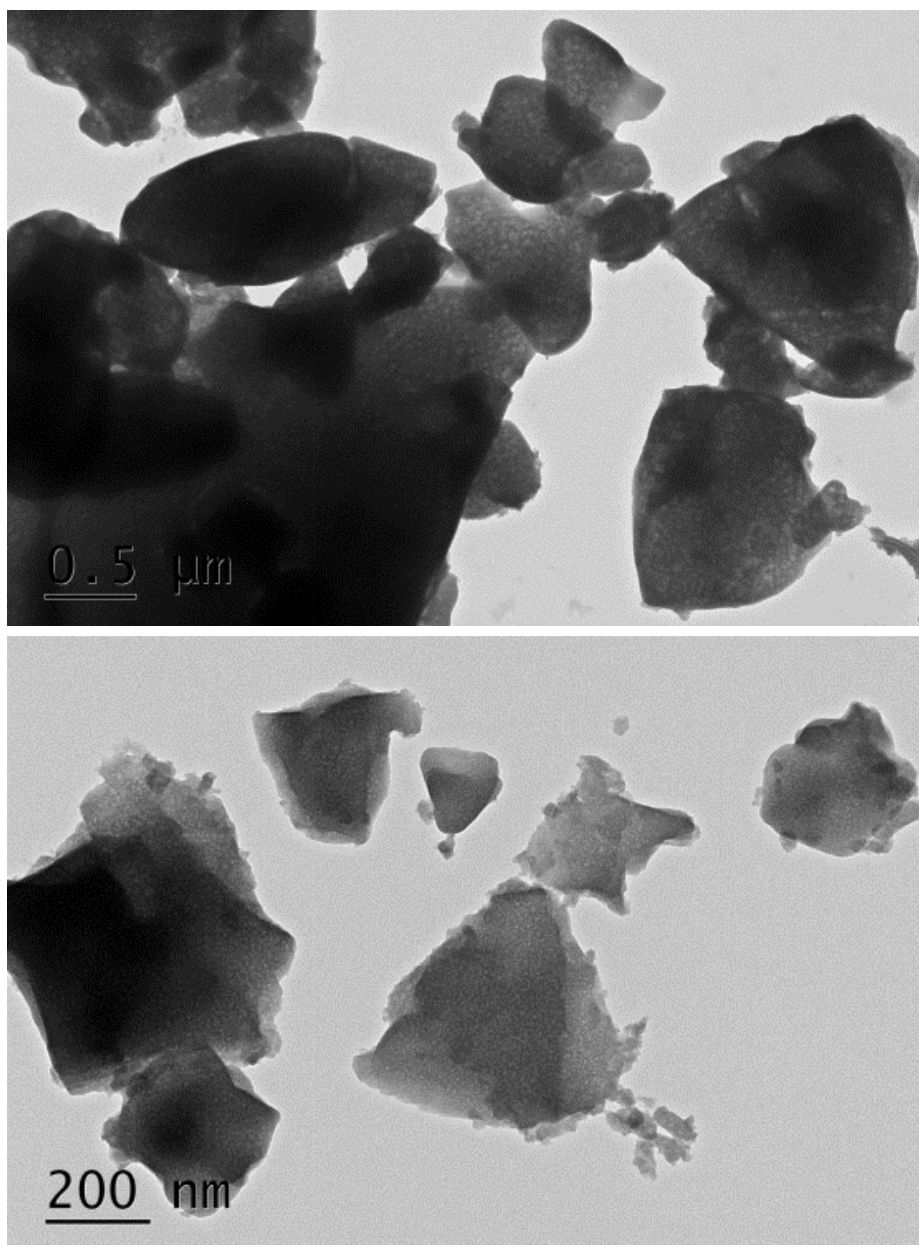
Figure S14. The SEM pictures of polycrystalline samples (Large crystals are too big to get the picture, and only same small ones are shown here. top) and ground samples (bottom). Related to Figure 2.
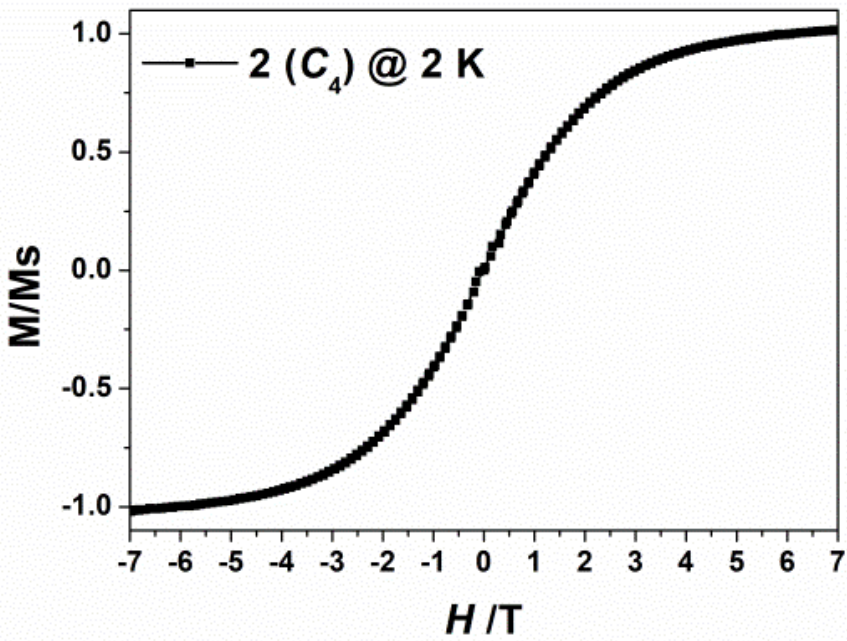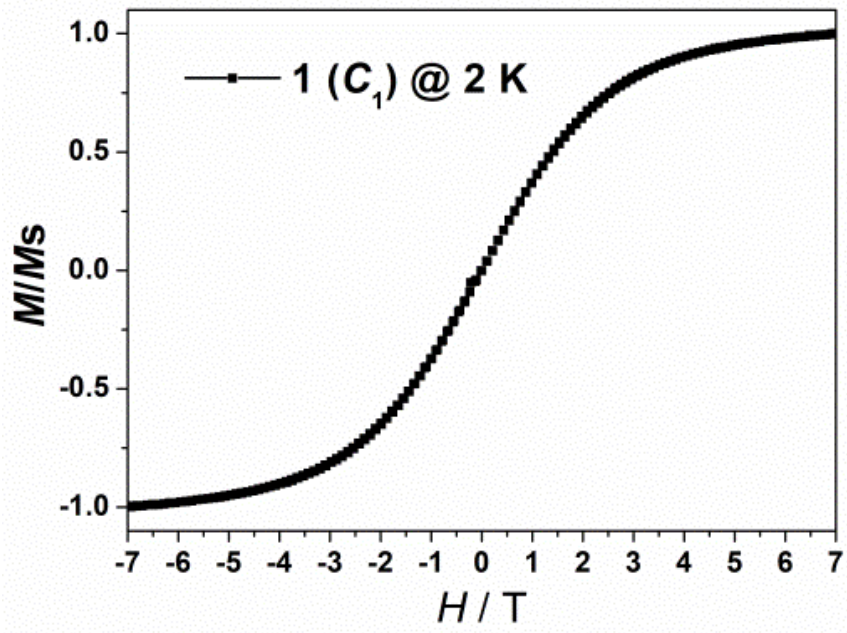
Figure S15. The magnetization curves for testing the magnetic hysteresis loops at 2 K using a VSM SQUID spectrometer by scanning the field at 100 Oe/s. Related to Figure 3.
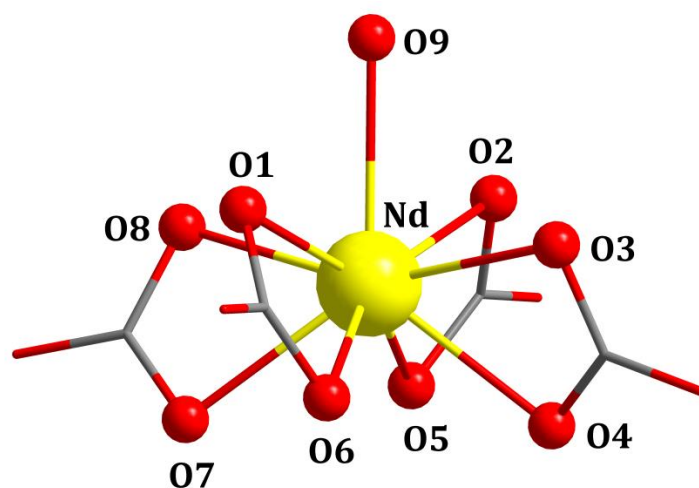
Figure S16. Calculated complete structures of complex **1** and **2**. H atoms are omitted. Related to Figure 1.
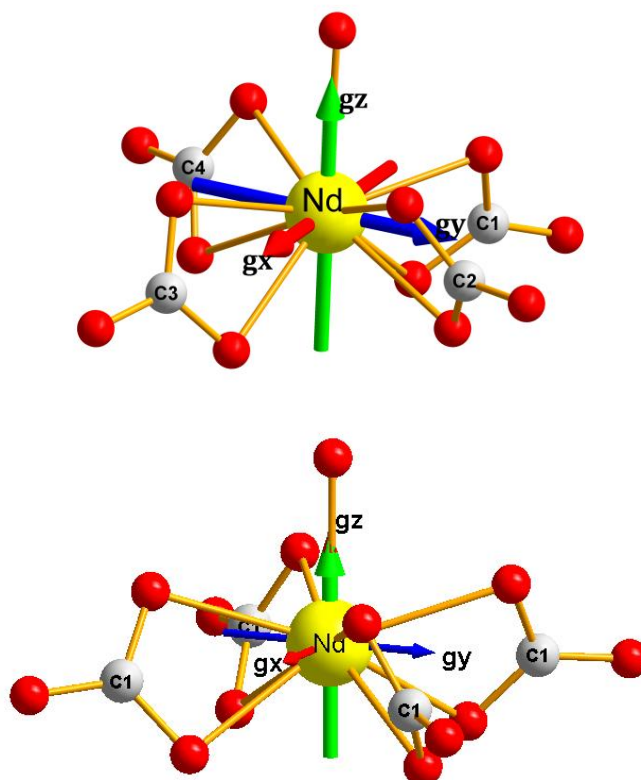
Figure S17. The calculated magnetic axes of complexes **1** (top) and **2** (bottom). Related to Figure 1.
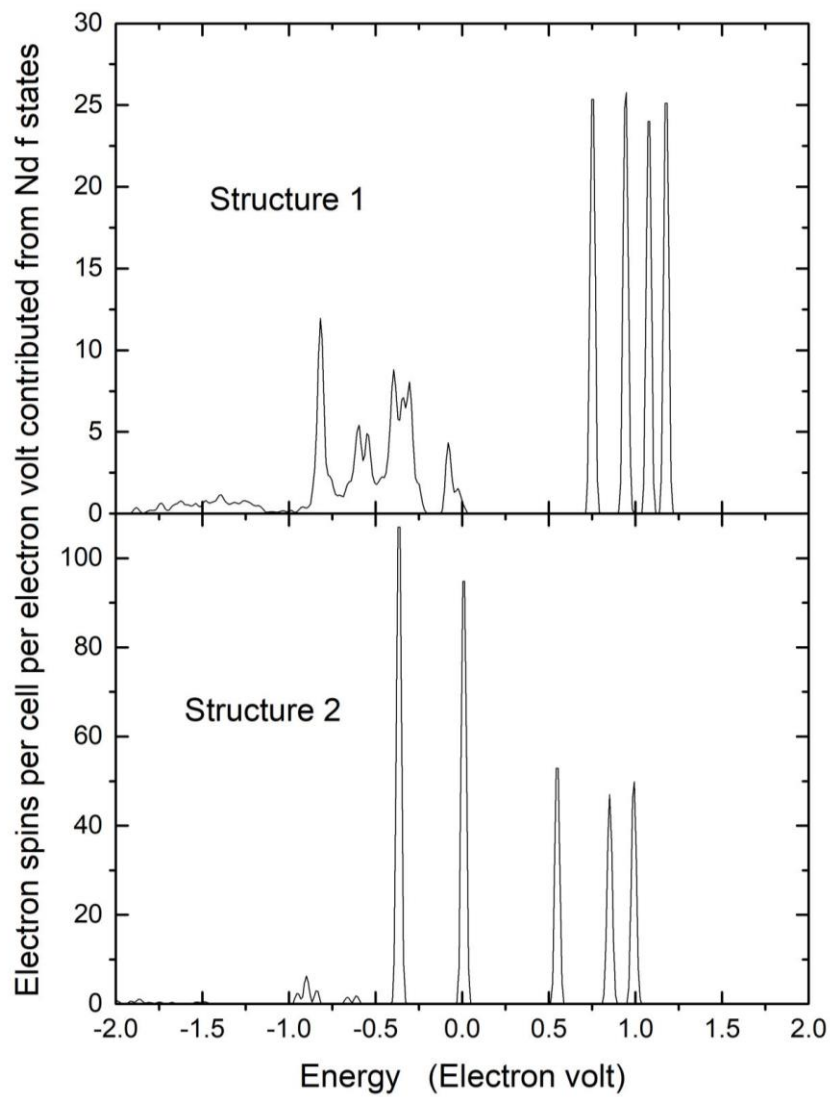
Figure S18. The calculated spins contributed from the *f* states of Nd ion as a function of energy for structures **1** and **2**. Related to Figure 5.

Supplemental tables

Table S1. Crystallographic data for complexes **1** and **2**.

	1	2
Formula	$C_9H_{36}N_{15}NdO_{15}$	$C_8H_{48}N_{12}NdO_{23.5}$
Mr[gmol^{-1}]	738.77	831.81
Crystal system	orthorhombic	tetragonal
Space group	$Pna2_1$	$P4/n$
a[Å]	21.438(4)	15.4630(9)
b[Å]	6.8275(15)	15.4630(9)
c[Å]	18.884(4)	7.5302(4)
α[º]	90.00	90
β[º]	90.00	90
γ[º]	90.00	90
V[Å^3]	2764.0(10)	1800.5(2)
T [K]	153	153
Z	4	2
ρ_{calcd} /g cm^{-3}	1.775	1.534
data measured	22530	14734
indep reflns	6776	9928
R_{int}	0.0516	0.0310
reflnswith I>2s(I)	6529	1953
parameter	363	140
Restraints	1	21
R1, wR2	0.0308 0.0767	0.0414 0.1155
GOF	1.065	1.193
CCDC	1546890	1860144

Table S2. Selected bond lengths (Å) and angles (°) for **1**. Related to Figure 1.

Nd-O1	2.542(4)	Nd-O2	2.466(4)
Nd-O4	2.489(4)	Nd-O5	2.470(4)
Nd-O7	2.511(4)	Nd-O8	2.462(4)
Nd-O10	2.483(4)	Nd-O11	2.455(4)
Nd-O13	2.622(5)		
O1-Nd-O2	52.53	O4-Nd-O5	53.31
O7-Nd-O8	52.94	O10-Nd-O11	53.14
O2-Nd-O13	71.2	O5-Nd-O13	77.31
O8-Nd-O13	68.54	O11-Nd-O13	78.64
C1-Nd-C2	89.90	C2-Nd-C3	86.51
C3-Nd-C4	89.75	C4-Nd-C1	90.59
C1-Nd-C3	172.49	C2-Nd-C4	154.01

Table S3. Selected bond lengths (Å) and angles (°) for **2**. Related to Figure 1.

Nd1-O1	2.507(3)	Nd1-O2	2.475(3)
Nd1-O4	2.431(7)		
O4-Nd1-O2	73.10(8)	O2-Nd1-O2^i	85.15(4)
O4-Nd1-O1	119.92(7)	O1-Nd1-O2	52.34(1)
O1-Nd1-O1^i	75.60(7)		

Table S4. Analysis of Cole-Cole plot of **1** under 1500 Oe *dc* field. Related to Figure 2.

T/K	χ_S	χ_t	T	α	R
1.8	1.39E-02	3.34E-01	4.39E-03	2.98E-01	4.36E-04
2.0	1.37E-02	3.03E-01	3.25E-03	2.98E-01	4.85E-04
2.2	1.48E-02	2.76E-01	2.41E-03	2.84E-01	4.48E-04
2.4	1.46E-02	2.55E-01	1.88E-03	2.83E-01	4.53E-04
2.6	1.80E-02	2.36E-01	1.51E-03	2.64E-01	4.53E-04
2.8	1.96E-02	2.17E-01	1.16E-03	2.39E-01	3.91E-04
3.0	2.11E-02	2.03E-01	9.20E-04	2.21E-01	2.94E-04
3.2	2.41E-02	1.92E-01	7.33E-04	1.88E-01	4.16E-04
3.4	2.20E-02	1.80E-01	5.37E-04	1.72E-01	3.08E-04
3.6	2.56E-02	1.70E-01	4.16E-04	1.33E-01	1.09E-04
3.8	2.77E-02	1.60E-01	3.12E-04	9.43E-02	1.55E-04
4.0	2.53E-02	1.54E-01	2.27E-04	8.79E-02	7.36E-05
4.2	2.42E-02	1.46E-01	1.61E-04	6.66E-02	1.02E-04
4.4	2.09E-02	1.39E-01	1.13E-04	5.49E-02	4.25E-05
4.6	5.10E-04	1.34E-01	6.67E-05	6.86E-02	6.69E-05
4.8	2.56E-15	1.28E-01	4.82E-05	4.59E-02	4.88E-05
5.0	5.01E-15	1.23E-01	3.71E-05	1.43E-03	8.19E-05
5.3	1.30E-14	1.17E-01	2.29E-05	1.43E-15	7.48E-05
5.6	2.13E-14	1.11E-01	1.43E-05	1.97E-15	6.49E-05

Table S5. Analysis of Cole-Cole plot of **2** under 1500 Oe *dc* field. Related to Figure 2.

T/K	χ_S	χ_t	T	α	R
1.8	5.54E-10	3.60E-01	2.91E-04	2.32E-01	1.48E-03
2	8.46E-10	3.27E-01	1.94E-04	2.30E-01	8.62E-04
2.2	1.13E-09	3.01E-01	1.37E-04	2.27E-01	1.24E-03
2.4	1.14E-09	2.79E-01	9.85E-05	2.19E-01	6.96E-04
2.6	1.67E-09	2.59E-01	7.43E-05	1.88E-01	2.57E-04
3	2.01E-09	2.29E-01	4.57E-05	1.54E-01	1.08E-04

Table S6. Calculated energy levels (cm⁻¹) and g (g_x, g_y, g_z) tensors of the lowest five Kramers doublets (KDs) of complex **1** and **2** calculated within CASSCF, respectively. Related to Figure 2.

KDs	1			2		
	CASSCF			CASSCF		
	E/cm⁻¹	g		E/cm⁻¹	g	
1	0.0	g_x	3.105	0.0	g_x	3.122
		g_y	3.017		g_y	3.071
		g_z	0.868		g_z	1.314
2	99.5	g_x	1.180	128.65	g_x	3.434
		g_y	1.500		g_y	2.964
		g_z	3.000		g_z	0.480
3	179.0	g_x	0.918	175.6	g_x	2.668
		g_y	1.217		g_y	2.636
		g_z	3.018		g_z	2.143
4	361.6	g_x	3.288	391.6	g_x	1.366
		g_y	2.111		g_y	1.423
		g_z	0.649		g_z	3.875
5	475.4	g_x	3.330	495.1	g_x	2.217
		g_y	2.548		g_y	2.419
		g_z	1.495		g_z	2.784

Table S7. In wave functions with definite projection of the total moment $|J_M>$ for complex **1** and **2** calculated within CASSCF and CASPT2, respectively. Related to Figure 2.

KDs	1		2	
	CASSCF		CASSCF	
	E/cm^{-1}	wave functions	E/cm^{-1}	wave functions
1	0.0	50%$|\pm5/2>$+46%$|\pm3/2>$	0.0	57.36%$|\pm5/2>$+42.59%$|\pm3/2>$
2	99.5	10%$|\pm9/2>$+34%$|\pm5/2>$+ 27%$|\pm3/2>$+28%$|\pm1/2>$	128.65	42.23%$|\pm5/2>$+56.99%$|\pm3/2>$ +
3	179.0	17%$|\pm9/2>$+9%$|\pm7/2>$ +13%$|\pm5/2>$+21%$|\pm3/2>$ +40%$|\pm1/2>$	175.6	37.44%$|\pm9/2>$+60.29%$|\pm1/2>$
4	361.6	15%$|\pm9/2>$+78%$|\pm7/2>$	391.6	12.64%$|\pm9/2>$+84.74%$|\pm7/2>$
5	475.4	57%$|\pm9/2>$+11%$|\pm7/2>$ 30%$|\pm1/2>$	495.1	49.54%$|\pm9/2>$+13.75%$|\pm7/2>$ +36.68%$|\pm1/2>$

Table S8. Literature survey for the SMMs based on light 4*f* elements. Related to Figure 2.

| Metal ion | Formula | Anisotropy | | E/k_B | τ_0 /s | H_{dc} /kOe | Refs. |
		Easy axis	Easy plane				
Ce³⁺	Ce(NO₃)₃(18-crown-6)[a]	√		30.3	2.20×10^{-7}	1.0	1
	Ce(NO₃)₃(1,10-diaza-18-crown-6)[a]	√		30.9	2.2×10^{-9}	1.0	1
	[Ce(NO₃){Zn(L1)(SCN)}₂]·CH₃CN	√		35.7	2.2×10^{-7}	1.0	2
	[Ce (COT′′)₂][Li(THF)₄]		√	30	1.2×10^{-6}	0.4	3, 4
	[Ce{ZnI(L)}₂(MeOH)]BPh₄·2MeOH·actone	√		21.2	1.6×10^{-7}	0	3,5
	[Ce{Zn(L)(AcO)}₂]BPh₄	√		37	2.7×10^{-7}	1.0	6
	[Ce(dmso)₈][Ce(η²-NO₃)₂(dmso)4(α-Mo₈O₂₆)₀.₅][Mo₆O₁₉]	-	-	24.4	2.56×10^{-7}	0.2	7
				4.4	2.09×10^{-5}		
				9.7	1.12×10^{-6}	1.4	
Nd³⁺	Nd(NO₃)₃(18-crown-6)	√		45	2.6×10^{-8}	1.0	1
	Nd(NO₃)₃(1,10-diaza-18-crown-6)	√		73	1.4×10^{-10}	1.0	1
	[Nd(NO₃){Zn(L1)(SCN)}₂]·CH₃CN	√		38.5	2.07×10^{-7}	1.0	2
	[L₂Nd(H₂O)₅][I]₃·L₂·(H₂O) (L=tBuPO(NHi-Pr)₂)	√		24.69	5.03×10^{-6}	0	8
				16.08	2.64×10^{-4}	0	
				39.21	8.98×10^{-7}	2.0	
	Na₉[Nd(W₅O₁₈)₂]·32H₂O	√		74.1	3.55×10^{-10}	1.0	9
	[Nd(COT′′)₂][Li(THF)₄]	-	-	21	5.5×10^{-5}	1.0	10
	[C(NH₂)₃]₅[Nd(CO₃)₄(H₂O)]·2H₂O		√	30.7	1.05×10^{-7}	1.5	**This work**
	[C(NH₂)₃]₄[Nd(CO₃)₄H₂O]·H₃O·13H₂O		√	7.7	3.97×10^{-6}	1.5	**This work**

Transparent Methods

(1).Experimental section

Complex **1**: Guanidine carbonate (4.5 g) was dissolved in 10 mL of distilled water. To this was added $Nd(NO_3)_3 \cdot 6H_2O$ (0.5 g) in 5mL distilled water. Precipitate formed, and ten minutes later it was filtered off. The resulting clear solution was stored in refrigerator and the block crystals were obtained after three days. Elemental analysis: found (calcd for Nd4C36O60H144N60)/%: C 14.63 (14.64), H 4.91 (4.76), N 28.44 (28.35). IR (cm-1, KBr): 3500(vs), 3116(vs), 2815(m), 2352(w), 2242(w), 1682(vs), 1564(s), 1461(s), 1373(vs), 1163(m), 868 (s), 757 (m), 711(m), 558(m)

Complex **2**: Guanidine carbonate (4.5 g) was dissolved in 10 mL of distilled water. To this was added $Nd(SO_3CF_3)_3$ (1 g) in 5mL distilled water. Precipitate formed, and ten minutes later it was filtered off. The resulting clear solution was stored in refrigerator and the block crystals were obtained after a week. The block crystal can stable in the room temperature for 5-10 min, but it is stable during several weeks below 270 K.

(2).Physical measurements.

The IR spectra were carried out using a Nexus 870 FT-IR spectrometer with KBr pellets in the range from 500 to 4000 cm−1. Elemental analyses of C, N, H were measured on a Perkin Elmer 240C elemental analyzer. Thermogravimetric analyses (TGA) were performed on a STA449F3 TG-DSC instrument in flowing N2 at a heating rate of 5 °C per minute in the range of 25 to 600 °C. The static magnetic measurements were collected on MPMS-XL7 SQUID magnetometer. The alternating-current (ac) susceptibility measurements were collected on a Quantum Design VSM SQUID magnetometer. The static magnetic measurements were performed in the temperature range 1.8-300 K in a field of 1000 Oe and the magnetization isothermal measurements were performed in fields of between 0 and 7 T on a polycrystalline sample. The alternating-current (ac) susceptibility measurements were carried out under an oscillating field of 2 Oe with frequency ranging from 1 to 999 Hz. Experimental susceptibilities were corrected for diamagnetism using Pascal's constants and for the sample holder by previous calibration. Pulsed high-field magnetization and HF-EPR measurements were performed on locally developed instruments at the Wuhan National High Magnetic Field Center in China. Pulsed HF-EPR measurements were done on a super-heterodyne EPR spectrometer at the National High Magnetic Field Laboratory in USA. The raw spectra obtained in an absorptive mode were subsequently digitally transformed into a derivative presentation.

(3).Crystallographic data collection and refinement.

Crystallographic data of complexes **1** and **2** were collected on Bruker APEX-II CCD area-detector diffractometer with Mo-Kα radiation (λ = 0.71073 Å) using an φ and ω scans at low temperature. The diffraction data were integrated using SAINT,[11a] and were corrected for absorption using SADABS.[11b] All non-hydrogen atoms were located by the Patterson method.[11c] The structures were solved by direct methods and refined using the full-matrix least-squares technique within the SHELXTL program package.[11d] All non-hydrogen atoms

were refined with anisotropic displacement parameters. The hydrogen atoms were generated geometrically using the riding-model.

(4).Theoretical calculations mothed

Complete active space second-order multiconfigurational perturbation theory (CASPT2) considering the effect of the dynamic electron correlation based on complete-active-space self-consistent field (CASSCF) method with MOLCAS 8.0 program package was performed on Nd^{3+} fragment (see Figure S15 for the calculated complete structure) on the basis of X-ray determined geometry of complex **1** and **2**. For CASSCF calculations, the basis sets for all atoms are atomic natural orbitals from the MOLCAS ANO-RCC library: ANO-RCC-VTZP for Nd^{3+} ion; VTZ for close O; VDZ for distant atoms. The calculations employed the second order Douglas-Kroll-Hess Hamiltonian, where scalar relativistic contractions were taken into account in the basis set. The effect of the dynamical electronic correlation was applied using CASPT2 based on the first CASSCF calculation. After that, the spin-orbit coupling was handled separately in the restricted active space state interaction (RASSI-SO) procedure. The active electronsin 7 active spaces include all *f* electrons (CAS(3 in 7) for complex **1**)in the CASSCF calculation. To exclude all the doubts we calculated all the roots in the active space. We have mixed the maximum number of spin-free state which was possible with our hardware (all from 35 sextets and 80 from 112 doublets).

In order to investigate the origin of the difference in the spin relaxation rate between **1** and **2**, we perform the first principles calculation on the spin polarization and corresponding electron orbitals using the generalized gradient approximation (GGA) of the Perdew, Burke, and Ernzerholf (PBE) form[12] under package CASTEP[13] in which a plane-wave norm-conserving pseudopotential Method[14] is adopted. The obtained spins contributed from Nd *f* states as functions of energy for structures **1** and **2** are plotted in Figure S17. From the curves we can see that the spin states in structure **1** are connected to continuous bands, while the spin states in structure **2** are more isolated to separated levels. This implies that the states in **1** are more extended in the space and the states in **2** are more isolated to the Nd atoms. The extended states are more easily influenced by the environment, especially by the spin relaxation processes due to the spin-orbit interaction plus phonons. For the sake of illustration in Figure 5 we plot the spatial distributions of the spin states at the Fermi level in Nd atom and its 4 ligands for both **1** and **2**. Compared with the extended feature of the states in **1**, the states in **2** are so isolated that they even could not be extended to the nearest ligands of the Nd atom.

Supplemental References

1. Wada, H.; Ooka, S.; Yamamura, T.; Kajiwara, T. Light Lanthanide Complexes with Crown Ether and Its Aza Derivative Which Show Slow Magnetic Relaxation Behaviors. *Inorg. Chem.* **2017**, 56, 147-155.

2. Takehara, C.; Then, P. L.; Kataoka, Y.; Nakano, M.; Yamamura, T.; Kajiwara, T. Slow Magnetic Relaxation of Light Lanthanide-based Linear $LnZn_2$ Trinuclear Complexes. *Dalton Trans.* **2015**, *44*, 18276-18283.

3. Singh, S. K.; Gupta, T.; Ungur, L.; Rajaraman, G. Magnetic Relaxation in Single-Electron Single-Ion Cerium(III) Magnets: Insights from Ab Initio Calculations. *Chem.-Eur. J.* **2015**, *21*, 13812-13819.

4. Le Roy, J. J.; Korobkov, I.; Kim, J. E.; Schelter, E. J.; Murugesu, M. Structural and Magnetic Conformation of a Cerocene $[Ce(COT'')_2]^-$ Exhibiting a Uniconfigurational f^1 Ground State and Slow-magnetic Relaxation. *Dalton Trans.* **2014**, *43*, 2737-2740.

5. Hino, S.; Maeda, M.; Yamashita, K.; Kataoka, Y.; Nakano, M.; Yamamura, T.; Nojiri, H.; Kofu, M.; Yamamuro, O.; Kajiwara, T. Linear Trinuclear Zn(ii)–Ce(iii)–Zn(ii) Complex Which Behaves as a Single-molecule Magnet. *Dalton Transactions* **2013**, *42*, 2683-2686.

6. Hino, S.; Maeda, M.; Kataoka, Y.; Nakano, M.; Yamamura, T.; Kajiwara, T. SMM Behavior Observed in $Ce(III)Zn(II)_2$ Linear Trinuclear Complex. *Chem. Lett.* **2013**, *42*, 1276-1278.

7. Khélifa, A. B.; Belkhiria, M. S.; Huang, G.; Freslon, S.; Guillou, O.; Bernot, K. Single-molecule Magnet Behaviour in Polynuclear Assembly of Trivalent Cerium Ions with Polyoxomolybdates. *Dalton Trans.* **2015**, *44*, 16458-16464.

8. Gupta, S. K.; Rajeshkumar, T.; Rajaraman, G.; Murugavel, R. An Unprecedented Zero Field Neodymium(iii) Single-ion Magnet Based on a Phosphonic Diamide. *Chem. Commun.* **2016**, *52*, 7168-7171.

9. Baldoví, J. J.; Clemente-Juan, J. M.; Coronado, E.; Duan, Y.; Gaita-Ariño, A.; Giménez-Saiz, C. Construction of a General Library for the Rational Design of Nanomagnets and Spin Qubits Based on Mononuclear *f*-Block Complexes. The Polyoxometalate Case. *Inorg. Chem.* **2014**, *53*, 9976-9980.

10. Le Roy, J. J.; Gorelsky, S. I.; Korobkov, I.; Murugesu, M. Slow Magnetic Relaxation in Uranium(III) and Neodymium(III) Cyclooctatetraenyl Complexes. *Organometallics* **2015**, *34*, 1415-1418.

11. (a) Madison, W. SAINT v5.0–6.01, Bruker Analytical X-ray Systems Inc, 1998. (b) Sheldrick, G. M. SADABSs: An Empirical Absorption Correction Program, 1996. (c) Patterson, A. L. A Fourier Series Method for the Determination of the Components of Interatomic Distances in Crystals. Phys. Rev. 1934, 46, 372-376. (d) SHELXTL 6.10, Bruker Analytical Instrumentation: Madison, WI, 2000.

12. Perdew, J. P.; Burke, K.; Ernzerhof, M. Generalized Gradient Approximation Made Simple. *Phys. Rev. Lett.* **1996**, *77*, 3865-3868.

13. Clark, S. J.; Segall, M. D.; Pickard, C. J.; Hasnip, P. J.; Probert, M. J.; Refson, K.; Payne, M. C. First Principles Methods Using CASTEP. *Z. Kristallogr.* **2005**, *220*, 567-570.

14. Hamann, D. R.; Schluter, M.; Chiang, C. Norm-Conserving Pseudopotentials. *Phys. Rev. Lett.* **1979**, *43*, 1494-1497.